Controlling the qubit-qubit coupling in the superconducting circuit with double-resonator couplers

Hui Wang [1,2,*] Yan-Jun Zhao [3,†] Hui-Chen Sun,[4] Xun-Wei Xu [5] Yong Li,[1,2]
Yarui Zheng,[6,‡] Qiang Liu,[1,2] and Rengang Li[1]

[1]*Shandong Inspur Intelligence Research Institute Co., Ltd., Jinan 250100, China*
[2]*Shandong Yunhai Guochuang Innovative Technology Co., Ltd., Jinan 250101, China*
[3]*Key Laboratory of Opto-electronic Technology, Ministry of Education, Beijing University of Technology, Beijing 100124, China*
[4]*Institute for Quantum Computing and Department of Physics and Astronomy, University of Waterloo, Waterloo, Ontario N2L 3G1, Canada*
[5]*Key Laboratory of Low-Dimensional Quantum Structures and Quantum Control of Ministry of Education, Key Laboratory for Matter Microstructure and Function of Hunan Province, Department of Physics and Synergetic Innovation Center for Quantum Effects and Applications, Hunan Normal University, Changsha 410081, China*
[6]*Quantum Element Technology (Shen Zhen) Co., Ltd., Shenzhen 518048, China*

(Received 1 May 2023; accepted 30 November 2023; published 2 January 2024)

We propose a theoretical scheme of using two fixed-frequency resonator couplers to tune the interaction between two Xmon qubits. The indirect interaction between two qubits induced by two resonators can cancel each other, so direct qubit-qubit coupling is not essential for the switching off. So, we can suppress the static ZZ coupling with the weak direct qubit-qubit coupling and even eliminate the static ZZ coupling through the destructive interferences of the double-path couplers. The cross-Kerr resonance can induce additional poles for the static ZZ coupling which should be kept away during the two-qubit gates. The double-resonator couplers scheme could unfreeze some restrictions during the design of superconducting quantum chips and mitigate the static ZZ coupling, which might supply a promising platform for future superconducting quantum chips.

DOI: 10.1103/PhysRevA.109.012601

I. INTRODUCTION

In the past several years, superconducting quantum computing has developed quickly. IBM announced a 433-qubit superconducting quantum chip at the end of 2022, and plans to launch a quantum chip with more than 1000 qubits in 2023. The coherence time of superconducting qubits fabricated with new superconducting materials is greatly enhanced [1–5], and the introduction of a tunable coupler greatly enhances the fidelities of two-qubit gates to above 99.5% [6–12]. Quantum supremacy of random circuit sampling and other multibody quantum simulation experiments has been conducted on the superconducting quantum chip with more than 50 qubits [4,13–15]. But the fidelities of the two-qubit gate are still not high enough for the universal quantum computer, and state leakages and residual coupling still need to be suppressed in the superconducting quantum chip.

The tunable coupler can switch off the interactions between adjacent qubits, which can isolate qubits from the surrounding environments for local quantum operations. In the single-coupler circuit, the induced indirect qubit-qubit coupling (dispersive type interaction) cannot be zero for finite frequency detuning between the qubit and coupler, so the direct qubit-qubit interaction is required for switching off. If the direct qubit-qubit coupling is very weak, the switching off frequency should be very high, and this leaves narrow available frequency ranges for readout resonators (or qubits). For the case of strong direct qubit-qubit coupling, the state leakages and crosstalks should be another may be another challenge [6–8]. So, there are many limitations during the design of a single-coupler superconducting quantum chip, and the residual coupling and state leakages are still serious problems [16].

In this article, we propose a theoretical scheme to dynamically tune the qubit-qubit coupling with double-resonator couplers in the superconducting quantum chip. As theoretically and experimentally demonstrated, the superconducting resonator can function as a coupler [10,17–21]. In particular, if the two resonator couplers take the respective maximal and minimal frequencies, the induced indirect qubit-qubit couplings by two resonators are in opposite signs and can cancel each other. So, direct qubit-qubit coupling is not indispensable for switching off in the double-resonator coupler circuit, which can hopefully unfreeze some restrictions on the superconducting quantum chip, such as the qubit-qubit coupling strength, maximal frequency of couplers, and so on. The switching off positions can be very close to two-qubit gate regimes in the double-resonator couplers circuit, thus the maximal frequencies of couplers can be smaller. So, available frequency ranges for readout resonators or qubits can be wider in a double-path coupler circuit, and this should relieve the frequency crowding on the superconducting quantum chip.

We also study the effects of a superconducting artificial atom's highly excited states on qubits' energy levels and switching off positions. The elimination of static ZZ coupling through the destructive interferences of double-path couplers

*wanghuiphy@126.com
†zhao_yanjun@bjut.edu.cn
‡ricezheng@qelement.xyz

 ©2024 American Physical Society

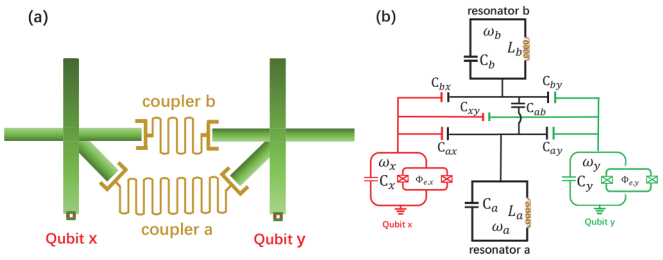

FIG. 1. (a) Schematic diagram. The double-resonator coupler superconducting circuit consists of two Xmon qubits coupled to two common fixed-frequency resonators. (b) The equivalent circuit. The ω_η is the frequency of a qubit or resonator, with $\eta = a, b, x, y$. The inductive-type coupling is neglected, and there are only capacitive-type interactions in the superconducting circuit. C_η is the capacitance of a qubit or resonator, and the two-body relative capacitance is $C_{\eta\eta'}$, with $C_{\eta\eta'} = C_{\eta'\eta}$ and $\eta \neq \eta'$. L_a and L_b are the respective inductances of resonators **a** and **b**, while $\Phi_{e,x}$ and $\Phi_{e,y}$ are the external magnetic fluxes applying on the superconducting loops of qubits **x** and **y**, respectively.

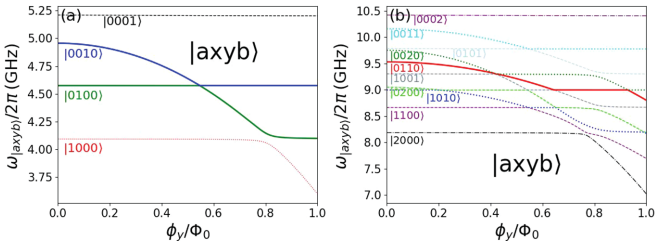

FIG. 2. The energy-level diagram. The energy-level curves for (a) single- and (b) double-excited states, where we set the transition frequency of qubit **x** as $\omega_x/2\pi = 4.56$ GHz. The maximal frequencies of qubits **x** and **y** are respectively $\omega_x^{(\max)}/2\pi = 4.56$ GHz and $\omega_y^{(\max)}/2\pi = 5.12$ GHz, and their corresponding anharmonicities are $\alpha_x/2\pi = -175$ MHz and $\alpha_y/2\pi = -195$ MHz. The resonant frequencies of resonators **a** and **b** are $\omega_a/2\pi = 4.10$ GHz and $\omega_b/2\pi = 5.20$ GHz, respectively. The direct qubit-qubit and direct resonator-resonator coupling strengths are $g_{xy}/2\pi = 1.0$ MHz and $g_{ab}/2\pi = 0.1$ MHz, respectively. The coupling strengths of qubits with resonator **a** are $g_{ax}/2\pi = g_{ay}/2\pi = 32$ MHz, and $g_{bx}/2\pi = g_{by}/2\pi = 30$ MHz label the coupling strengths of qubits with resonator **b**.

is also explored [12,22–24]. We find that the cross-Kerr resonances through the virtual photon exchange could induce new poles of static ZZ coupling, which should be kept away from during the two-qubit gates.

The paper is organized as follows: In Sec. II, we first perform numerical calculation of the circuit energy levels. In Sec. III, we then discuss the switching off for the qubit-qubit coupling. In Sec. IV, we further study the suppression and cancellation of static ZZ coupling. Finally, we summarize the results in Sec. V.

II. CIRCUIT ENERGY LEVELS

In this section, we numerically calculate the energy levels of qubits for the superconducting circuit in Fig. 1 with the QUTIP software [16,25–27]. The superconducting circuit consists of two Xmon qubits coupled to two common resonator couplers. The two-body interactions are all assumed as capacitive type, and the direct qubit-qubit and resonator-resonator interactions are very weak. The two-body interactions in the superconducting circuit are all assumed as capacitive type. Because of the small anharmonicities, the highly excited states of superconducting artificial atoms should also make contributions to the energy levels of qubits and couplers. Truncated to the second excited states of atoms and third excited states of resonators, the curved surfaces of qubits and resonators' energy levels are plotted in Appendix A (see Fig. 10).

For simplicity, we focus on the special case that the resonant frequency ω_a of resonator **a**, resonant frequency ω_b of resonator **b**, and transition frequency ω_x of qubit **x** are fixed, and only the transition frequency ω_y for qubit **y** is tuned by the external magnetic flux $\Phi_{e,y}$. By setting $\omega_x/(2\pi) = 4.56$ GHz, the energy-level curves of qubits and resonators' single- and double-excited states are plotted in Figs. 2(a) and 2(b), respectively. During the numerical calculations with QUTIP software, the transition frequencies of qubits **x** and **y** are respectively chosen as $\omega_x/(2\pi) = 4.56$ GHz and $\omega_y/(2\pi) = 5.12$ GHz, and the resonant frequencies of resonator **a** and resonator **b** are $\omega_a/(2\pi) = 4.10$ GHz and $\omega_b/(2\pi) = 5.20$ GHz, respectively. The coupling strengths between resonator **a** (or **b**) and two qubits are $g_{ax}/(2\pi) = g_{ay}/(2\pi) = 32$ MHz [or $g_{bx}/(2\pi) = g_{by}/(2\pi) = 30$ MHz], so the qubits and couplers are in the dispersive coupling regimes.

The ket vector of the four-body quantum state is defined as $|m_a m_x m_y m_b\rangle$, and the values of m_a, m_x, m_y, and m_b respectively describe quantum numbers of resonator **a**, qubit **x**, qubit **y**, and resonator **b**. Because of the avoided crossing effect, each curve in Fig. 2 cannot describe the whole energy level of a certain quantum state, so here we mark each curve with the corresponding state at the zero magnetic flux. In Fig. 2(a), the transition frequency of qubit **y** decreases under magnetic field, and it becomes anticrossing with qubit **x** at the frequency regimes close to 4.56 GHz and with resonator **a** at the regimes close to 4.10 GHz. For the double-excited states, the energy levels and avoided crossing gaps can be seen in Fig. 2(b). The energy-level structure in Fig. 2 is important for analyzing the switching off and static ZZ coupling on the superconducting quantum chip, as shown in the following sections.

III. SWITCHING OFF

A. Circuit quantization

Figure 1(a) describes the superconducting circuit consisting of two Xmon qubits coupling to two common fixed-frequency resonators, and the frequencies of the qubits are tunable. Besides the direct interactions, the qubit-resonator couplings can also induce indirect qubit-qubit and resonator-resonator interactions. The resonant frequencies of resonators **a** and **b** are respectively ω_a and ω_b, while ω_x and ω_y label the transition frequencies of qubits **x** and **y**, respectively. In the case of zero magnetic fluxes, the frequencies of qubits and resonators satisfy $\omega_a < \omega_x < \omega_y < \omega_b$. We expect a large distance between two resonators and neglect their inductive coupling, then the interactions are all regarded as capacitive type as shown in Fig. 1(b). The capacitances of resonators should be distributed by type and proportional to their lengths, but in the article we simply label the total capacitances of resonators **a** and **b** as C_a and C_b, respectively.

Inspired by previous work [17,20], the kinetic energy of a superconducting circuit with double-resonator couplers can be written as $T=\sum_{\eta=a,b,x,y} C_\eta\dot{\phi}_\eta^2/2+\sum_{\substack{\eta,\eta'=a,b,x,y\\ \eta\neq\eta'}} C_{\eta\eta'}(\dot{\phi}_\eta-\dot{\phi}_{\eta'})^2/4$, where C_η is the capacitance of the qubit or resonator, and $C_{\eta\eta'}$ ($C_{\eta\eta'}=C_{\eta'\eta}$) is the relative capacitance between two arbitrary devices among qubits and resonators, with $\eta,\eta'=a,b,x,y$ and $\eta\neq\eta'$. ϕ_a and ϕ_b are the respective magnetic fluxes of circuit nodes for resonators **a** and **b**, while ϕ_x and ϕ_y are the respective node fluxes of qubits **x** and **y**, and they can be tuned by the external magnetic fluxes $\Phi_{e,x}$ and $\Phi_{e,y}$ [28–30]. If we label L_a and L_b as the respective inductances of resonators **a** and **b**, then the potential energy of the superconducting circuit can be written as $U=\sum_{\lambda=a,b}\phi_\lambda^2/(2L_\lambda)+\sum_{\beta=x,y}E_{J_\beta}[1-\cos(2\pi\phi_\beta/\Phi_0)]$, where the subscript $\lambda=a,b$ label the respective variables of resonators **a** and **b**, while $\beta=x,y$ describe the variables of qubit **x** and qubit **y**, respectively. $E_{J_\beta}=I_{c\beta}\Phi_0/(2\pi)$ is the Josephson energy of qubit β, where $I_{c\beta}$ is the corresponding critical current, and $\Phi_0=h/2e$ is the flux quantum with the planck constant **h** and an electron charge **e**.

With the kinetic energy T and potential energy U, the Lagrangian of the superconducting circuit in Fig. 1 can be formally written as $L=T-U$. If we define the generalized momentum operators as $q_\eta=\partial L/\partial\dot{\phi}_\eta=C\dot{\phi}_\eta$ (with $\eta=a,b,x,y$), under the conditions $C_{ab}\ll C_{xy}\ll C_{ax},C_{ay},C_{bx},C_{by}\ll C_x,C_y\ll C_a,C_b$, we obtain the expression of Hamiltonian (see Appendix B)

$$\begin{aligned}H=&4\sum_{\lambda=a,b}\left[E_{C_\lambda}(n_\lambda)^2+\frac{\phi_\lambda^2}{8L_\lambda}\right]\\&+\sum_{\beta=x,y}\left[E_{C_\beta}(n_\beta)^2-E_{j\beta}\cos\left(\frac{2\pi}{\Phi_0}\phi_\beta\right)\right]\\&+8\sum_{\substack{\lambda=a,b\\ \beta=x,y}}\frac{C_{\lambda\beta}}{\sqrt{C_\lambda C_\beta}}\sqrt{E_{C_\lambda}E_{C_\beta}}(n_\lambda n_\beta)\\&+8\left(1+\frac{C_{ax}C_{bx}}{C_xC_{ab}}+\frac{C_{ay}C_{by}}{C_yC_{ab}}\right)\frac{C_{ab}}{\sqrt{C_aC_b}}\sqrt{E_{C_a}E_{C_b}}(n_an_b)\\&+8\left(1+\frac{C_{ax}C_{ay}}{C_aC_{xy}}+\frac{C_{bx}C_{by}}{C_bC_{xy}}\right)\frac{C_{xy}}{\sqrt{C_xC_y}}\sqrt{E_{C_x}E_{C_y}}(n_xn_y),\end{aligned}\tag{1}$$

where $n_\eta=q_\eta/2e$ is the Cooper-pair number operator of a qubit or resonator, and the corresponding charging energy is $E_{C_\eta}=e^2/2C_\eta$. The transition frequencies of resonators and qubits are respectively defined as $\omega_\lambda=1/\sqrt{C_\lambda L_\lambda}$ and $\omega_\beta=(\sqrt{8E_{J_\beta}E_{C_\beta}}-E_{C_\beta})/\hbar$, while $\alpha_\beta=-E_{C_\beta}/\hbar$ labels the anharmonicity of qubit β. As shown in Appendix B, the two-body coupling strengths among qubits and resonators can be defined as

$$g_{\lambda\beta}=\frac{1}{2}\frac{C_{\lambda\beta}}{\sqrt{C_\lambda C_\beta}}\sqrt{\omega_\lambda\omega_\beta},\tag{2}$$

$$g_{ab}=\frac{1}{2}\left(1+\frac{C_{ax}C_{bx}}{C_xC_{ab}}+\frac{C_{ay}C_{by}}{C_yC_{ab}}\right)\frac{C_{ab}}{\sqrt{C_aC_b}}\sqrt{\omega_a\omega_b},\tag{3}$$

$$g_{xy}=\frac{1}{2}\left(1+\frac{C_{ax}C_{ay}}{C_aC_{xy}}+\frac{C_{bx}C_{by}}{C_bC_{xy}}\right)\frac{C_{xy}}{\sqrt{C_xC_y}}\sqrt{\omega_x\omega_y}.\tag{4}$$

The two-body interactions are mainly decided by their relative capacitances $C_{\eta\eta'}$, with $\eta,\eta'=a,b,x,y$ and $\eta\neq\eta'$. The qubit-resonator coupling strength $g_{\lambda\beta}$ in Eq. (2) could induce an indirect interaction between two qubits, so Eq. (4) cannot describe the complete interaction between two qubits. In the single-coupler superconducting quantum chip, there are many restrictions on the capacitances and frequencies of qubits (or couplers), but these limitations might be unfrozen in the double-coupler circuit, as will be discussed in the follow sections.

B. Effective coupling

To get effective qubit-qubit coupling, we try to decouple the qubit-resonator interactions in this section. For the Xmon qubit, the Josephson energy is much larger than its charging energy, $E_{J_\beta}/E_{C_\beta}\gg 1$, and then the ϕ_β should be very small and we can use the approximate equation $\cos(\phi_\beta)=1-\phi_\beta^2/2+\phi_\beta^4/24-\cdots$. If we introduce the creation and annihilation operators by the definitions $\phi_\beta=\sqrt[4]{2E_C/E_{J_\beta}}(a_\beta^\dagger+a_\beta)$ and $n_\beta=(i/2)\sqrt[4]{2E_C/E_{J_\beta}}(a_\beta^\dagger-a_\beta)$, the second-quantization Hamiltonian can be obtained as $H=\sum_{\lambda=a,b}H_\lambda+\sum_{\beta=x,y}H_\beta+\sum_{\substack{\lambda=a,b\\ \beta=x,y}}H_{\lambda\beta}+H_{ab}+H_{xy}$, with

$$H_\lambda/\hbar=\frac{\omega_\lambda}{2}c_\lambda^\dagger c_\lambda,\tag{5}$$

$$H_\beta/\hbar=\frac{\omega_\beta}{2}a_\beta^\dagger a_\beta+\frac{\alpha_\beta}{2}a_\beta^\dagger a_\beta^\dagger a_\beta a_\beta,\tag{6}$$

$$H_{\lambda\beta}/\hbar=g_{\lambda\beta}(c_\lambda^\dagger a_\beta+c_\lambda a_\beta^\dagger-c_\lambda^\dagger a_\beta^\dagger-c_\lambda a_\beta),\tag{7}$$

$$H_{ab}/\hbar=g_{ab}(c_a^\dagger c_b+c_a c_b^\dagger-c_a^\dagger c_b^\dagger-c_a c_b),\tag{8}$$

$$H_{xy}/\hbar=g_{xy}(a_x^\dagger a_y+a_x a_y^\dagger-a_x^\dagger a_y^\dagger-a_x a_y).\tag{9}$$

We define $\alpha_\beta=-E_{C_\beta}/\hbar$ to describe the anharmonicity of qubit β, and the nonlinear term $(\alpha_\beta/2)a_\beta^\dagger a_\beta^\dagger a_\beta a_\beta$ reflects the effects of highly excited states of the superconducting artificial atom. We define $\Delta_{\lambda\beta}=\omega_\beta-\omega_\lambda$ to describe the frequency detuning between qubit β and resonator λ, while $\Sigma_{\lambda\beta}=\omega_\beta+\omega_\lambda$ is the frequency summation of qubit β and resonator λ. $\Delta_{xy}=\omega_y-\omega_x$ describes the frequency detuning between two qubits, and $\Delta_{ab}=\omega_b-\omega_a$ labels the frequency detuning between two resonators.

Separating the Hamiltonian as $H=H_0+H_{\rm int}$, the free term is defined as $H_0=\sum_{\lambda=a,b}H_\lambda+\sum_{\beta=x,y}H_\beta$, while the interaction term is $H_{\rm int}=H_{ab}+H_{xy}+\sum_{\substack{\lambda=a,b\\ \beta=x,y}}H_{\lambda\beta}$. In the qubit-resonator dispersive coupling regimes $g_{\lambda\beta}/|\Delta_{\lambda\beta}|\ll 1$ and $g_{\lambda\beta}/\Sigma_{\lambda\beta}\ll 1$, we define $S=\sum_{\substack{\lambda=a,b\\ \beta=x,y}}[(g_{\lambda\beta}/\Delta_{\lambda\beta})(c_\lambda^\dagger a_\beta-c_\lambda a_\beta^\dagger)-(g_{\lambda\beta}/\Sigma_{\lambda\beta})(c_\lambda^\dagger a_\beta^\dagger-c_\lambda a_\beta)]$. Under the Schrieffer-Wolff transformation, if we choose $H^{(d)}=\exp(S)H\exp(-S)$ and $H_{\rm int}+[S,H_0]=0$, then the decoupled Hamiltonian becomes $H^{(d)}=H_0-(1/2)[H_{\rm int},S]+O(H_{\rm int}^3)$ (see Appendix C), that is,

$$\begin{aligned}\frac{H^{(d)}}{\hbar}=&\sum_{\lambda=a,b}\omega_\lambda^{(d)}c_\lambda^\dagger c_\lambda+\sum_{\beta=x,y}\left(\omega_\beta^{(d)}a_\beta^\dagger a_\beta+\frac{\tilde{\alpha}_\beta}{2}a_\beta^\dagger a_\beta^\dagger a_\beta a_\beta\right)\\&+g_{xy}^{(d)}(a_x^\dagger a_y+a_y^\dagger a_x)+g_{ab}^{(d)}(c_a^\dagger c_b+c_b^\dagger c_a).\end{aligned}\tag{10}$$

Since $g_{ab}, g_{xy} \ll g_{\lambda\beta}$, the contributions of H_{ab} and H_{xy} have been neglected. Following the method of previous work [7], we assumed $\tilde{\alpha}_\beta \approx \alpha_\beta$ during the derivations of Eq. (10), thus the contributions of superconducting artificial atoms' highly excited states are neglected.

The decoupled frequencies of qubits and resonators can be respectively defined as $\omega_\beta^{(d)} = \omega_\beta + \sum_{\lambda=a,b}(g_{\lambda\beta}^2/\Delta_{\lambda\beta} - g_{\lambda\beta}^2/\Sigma_{\lambda\beta})$ and $\omega_\lambda^{(d)} = \omega_\lambda - \sum_{\beta=x,y}(g_{\lambda\beta}^2/\Delta_{\lambda\beta} - g_{\lambda x}^2/\Sigma_{\lambda\beta})$ (as shown in Appendix C), and the decoupled qubit-qubit coupling strength can be obtained as

$$g_{xy}^{(d)} = \frac{1}{2}\sum_{\substack{\lambda=a,b\\ \beta=x,y}}\left(\frac{g_{\lambda x}g_{\lambda y}}{\Delta_{\lambda\beta}} - \frac{g_{\lambda x}g_{\lambda y}}{\Sigma_{\lambda\beta}}\right) + g_{xy}. \tag{11}$$

Since $\Delta_{\lambda\beta}$ and $\Sigma_{\lambda\beta}$ depend on the frequency of qubit β, the induced qubit-qubit coupling $g_{\lambda,xy}^{(in)} = (1/2)\sum_{\beta=x,y}(g_{\lambda x}g_{\lambda y}/\Delta_{\lambda\beta} - g_{\lambda x}g_{\lambda y}/\Sigma_{\lambda\beta})$ can be tuned by the external magnetic fluxes $\Phi_{e,x}$ and $\Phi_{e,y}$. To switch off the qubit-qubit coupling $[g_{xy}^{(d)}/(2\pi) = 0$ Hz], we should find parameters to satisfy $-g_{xy}^{(in)} = g_{xy}$.

From the expression of $g_{\lambda,xy}^{(in)}$, both resonators make contributions to the effective qubit-qubit coupling, and their contributions might cancel each other out ($g_{a,xy}^{(in)} + g_{b,xy}^{(in)} = 0$) if the qubit frequency of qubits satisfies certain conditions. Thus, the direct qubit-qubit coupling might be not be necessary for the switching off in the double-resonator couplers circuit. The qubits could also induce indirect interactions between the two resonators, and the decoupled resonator-resonator coupling strength can be defined as $g_{ab}^{(d)} = (1/2)\sum_{\substack{\lambda=a,b\\ \beta=x,y}}(g_{a\beta}g_{b\beta}/\Delta_{\lambda\beta} - g_{a\beta}g_{b\beta}/\Sigma_{\lambda\beta}) + g_{ab}$ (see Appendix C). Because of the large frequency detuning between two resonators ($|\Delta_{ab}| \gg g_{ab}^{(d)}$), the effective resonator-resonator interaction has little effect on the energy levels of qubits and resonators.

With the parameters in Fig. 2, we can get $g_{by}/\min(|\Delta_{by}|) \sim 1/3$ and $g_{ax}/\min(|\Delta_{ax}|) \sim 1/15$ in the idling states of qubits (without external magnetic field). This means that the qubits and resonators are in the dispersive or weak-dispersive coupling regimes, thus the perturbation method can be used to calculate the effective qubit-qubit coupling. If we choose $\omega_a < \omega_x < \omega_y < \omega_b$, the signs of $\Delta_{a\beta}$ and $\Delta_{b\beta}$ are opposite. As indicated by $g_{\lambda,xy}^{(in)}$, resonator **b** will induce negative indirect qubit-qubit coupling, and the contribution of resonator **a** is positive. With Eq. (11), the curved surfaces of $g_{xy}^{(d)}$ are plotted in Figs. 3(a) and 3(c), and the corresponding decoupled frequencies of qubits are shown in Figs. 3(b) and 3(d). The curved surface of $g_{xy}^{(d)}$ has many crossing points with the zero-value plane $[g_{xy}^{(d)}/(2\pi) = 0$ Hz] in Fig. 3(a) $[g_{xy}/(2\pi) = 3$ MHz], which correspond to switching off positions for the qubit-qubit coupling. The multiple switching off points can be used to optimize the quantum operation parameters and reduce the effects of adjoint qubits. For the case of nonzero direct qubit-qubit coupling ($g_{xy} \neq 0$), the distribution of crossing points forms an approximately elliptical curve in the ϕ_x-ϕ_y plane as shown in Fig. 3(a), and this means that the contribution of resonator **b** to induced qubit-qubit coupling (in amplitudes) is larger than the contribution of resonator **a**.

In the case of $g_{xy}/(2\pi) = 0$ Hz, the effective qubit-qubit can also be zero if the indirect qubit-qubit couplings induced by resonators **a** and **b** are the same in amplitudes but opposite in signs ($g_{a,xy}^{(in)} = -g_{b,xy}^{(in)}$). As shown in Fig. 3(c), the curved surface of $g_{xy}^{(d)}$ can also cross with the zero-value plane $[g_{xy}^{(d)}/(2\pi) = 0$ Hz] in the case of $g_{xy}/(2\pi) = 0$ Hz, and this means that the switching off can be realized without the direct qubit-qubit interaction in the double-resonator couplers circuit. The distribution of switching off points approximately forms a circle in the ϕ_x-ϕ_y plane in Fig. 3(c), which indicates the approximate equal contributions (in amplitudes) of two resonators to the effective qubit-qubit couplings. The decoupled frequencies of qubits are plotted in Fig. 3(b) $[g_{xy}/(2\pi) = 3$ MHz] and Fig. 3(d) $[g_{xy}/(2\pi) = 0$ Hz], and the effects of direct qubit-qubit coupling to the transition frequencies of qubits seem not very large.

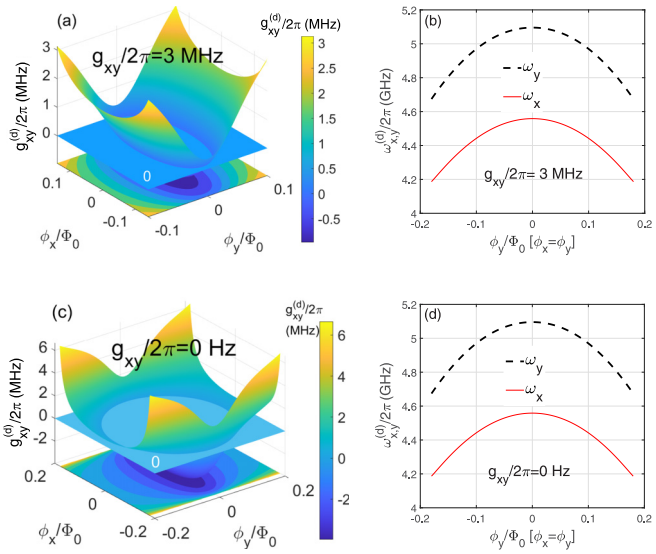

FIG. 3. The decoupled qubit-qubit coupling strengths. The curved surfaces of $g_{xy}^{(d)}$ are plotted in (a) $g_{xy}/2\pi = 3$ MHz and (c) $g_{xy}/2\pi = 0$ Hz, while (b) and (d) describe the corresponding decoupled frequencies of qubits along the diagonal line direction in the ϕ_x-ϕ_y plane. The other parameters are the same as in Fig. 2.

The switching off positions are not totally decided by the direct qubit-qubit coupling in the double-resonator coupler circuit, thus we can take arbitrary small or even zero direct qubit-qubit coupling strength in principle, which might be helpful to suppress the state leakages and crosstalks on the superconducting quantum chips. And the restrictions on the direct qubit-qubit coupling strength and coupler's frequency can be unfreezed on the double-resonator couplers superconducting quantum chip. If we choose the switching off positions close to two-qubit gate regimes, then the maximal frequencies of couplers can be smaller, and this might create wider available frequency ranges for the readout resonators and relieve the frequency crowding on the superconducting quantum chip.

C. Highly excited states corrections

In the current theoretical model for the tunable coupler circuit, the nonlinear term $H_{nl,\beta} = (\alpha_\beta/2)a_\beta^\dagger a_\beta^\dagger a_\beta a_\beta$ is regarded as invariant during dynamical decoupling processes

for qubit-resonator interactions [7,16]. This approximation in fact neglects the effects of superconducting artificial atoms' highly excited states, so the $g_{xy}^{(d)}$ in Eq. (11) does not contain the information of anharmonicity α_β. Because of the small anharmonicity for the Xmon qubit (between 200 MHz and 400 MHz), the interactions between the resonators and highly excited states of superconducting artificial atoms should make corrections to the qubits' energy levels and effective qubit-qubit coupling.

The Bogoliubov transformation has been used to analyze the variations of nonlinear term $H_{nl,\beta}$ during the decoupling processes [31,32], and the derived self-Kerr and cross-Kerr resonant terms under the unitary transformation reflect the contributions of superconducting artificial atoms' highly excited states. To maintain consistency, in this section we continue to use the Schrieffer-Wolff transformation to calculate the effects of the nonlinear term $H_{nl,\beta}$ (see Appendix D). In the qubit-resonator dispersive coupling regimes, $g_{\lambda\beta}/|\Delta_{\lambda\beta}| \ll 1$ and $g_{\lambda\beta}/|\Sigma_{\lambda\beta}| \ll 1$, we define $S_{\lambda\beta} = (g_{\lambda\beta}/\Delta_{\lambda\beta})(c_\lambda^\dagger a_\beta - c_\lambda a_\beta^\dagger) - (g_{\lambda\beta}/\Sigma_{\lambda\beta})(c_\lambda^\dagger a_\beta^\dagger - c_\lambda a_\beta)$ with $S = \sum_{\substack{\lambda=a,b \\ \beta=x,y}} S_{\lambda\beta}$. Since $H_{nl,\beta}$ is a small quantity, we will separately conduct the unitary transform $H'_{nl,\beta} = \exp(S) H_{nl,\beta} \exp(-S)$ to study its contributions to the high-order effects, such as cross-Kerr resonance, self-Kerr resonance, and so on [32]. With tedious calculations (see Appendix D), up to the second-order perturbation expansion terms, we get

$$H'_{nl,\beta} \approx \sum_{\lambda=a,b} \left(\frac{g_{\lambda\beta}^2 \alpha_\beta}{\Sigma_{\lambda\beta}^2} - \frac{g_{\lambda\beta}^2 \alpha_\beta}{\Delta_{\lambda\beta}^2} \right) a_\beta^\dagger a_\beta^\dagger a_\beta a_\beta + \sum_{\lambda=a,b} \left[\frac{2g_{\lambda x}^2 \alpha_\beta}{\Delta_{\lambda\beta}^2} c_\lambda^\dagger c_\lambda a_\beta^\dagger a_\beta + \frac{2g_{\lambda\beta}^2 \alpha_\beta}{\Sigma_{\lambda\beta}^2} c_\lambda c_\lambda^\dagger a_\beta^\dagger a_\beta \right]. \tag{12}$$

Since $g_{xy}, g_{ab} \ll g_{\lambda\beta}$, the indirect interaction induced by the weakly direct qubit-qubit and resonator-resonator interactions have been neglected. The first and second lines in the right side of Eq. (12) respectively describe the self-Kerr and cross-Kerr resonance terms, and the complete calculation results can be seen in Appendix D. There are no external pump fields for resonator couplers, so the cavity photon numbers should be very small ($n_\lambda = a_\lambda^\dagger a_\lambda \ll 1$). Thus, we can get the approximate frequency shift for qubit β induced by the nonlinear terms

$$\Delta\omega_\beta = \sum_{\lambda=a,b} \left(\frac{g_{\lambda\beta}^2}{\Delta_{\lambda\beta}^2} + \frac{g_{\lambda\beta}^2}{\Sigma_{\lambda\beta}^2} \right) \alpha_\beta. \tag{13}$$

We can see that the frequency shift $\Delta\omega_\beta$ for qubit β is proportional to the qubit's anharmonicity α_β, which reflects the effects of the second excited state of superconducting artificial atoms. Adding the frequency shift induced by the nonlinear term $H_{nl,\beta}$, we can approximately get the corrected frequency $\omega_\beta^{(cr)}$ of qubit β in a decoupled coordinate frame:

$$\omega_\beta^{(cr)} = \omega_\beta + \sum_{\lambda=a,b} \left(\frac{g_{\lambda\beta}^2}{\Delta_{\lambda\beta}} - \frac{g_{\lambda\beta}^2}{\Sigma_{\lambda\beta}} \right) + \sum_{\lambda=a,b} \left(\frac{g_{\lambda\beta}^2}{\Delta_{\lambda\beta}^2} + \frac{g_{\lambda\beta}^2}{\Sigma_{\lambda\beta}^2} \right) \alpha_\beta. \tag{14}$$

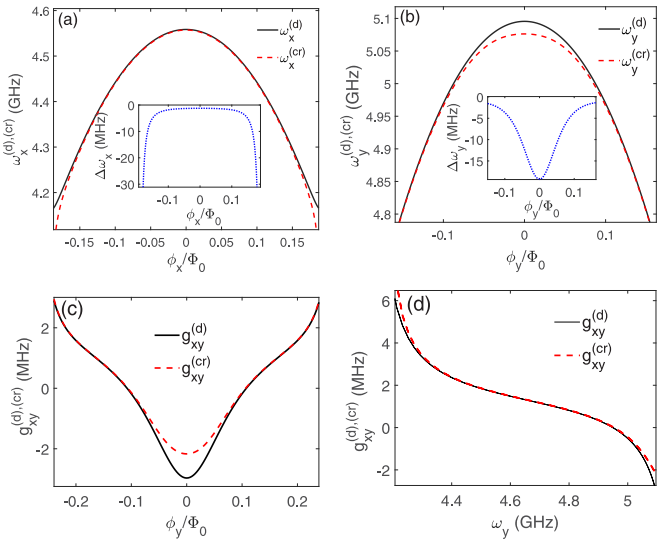

FIG. 4. Corrections by highly excited states. The black solid curves in (a) qubit **x** and (b) qubit **y** describe the decoupled frequencies $\omega_\beta^{(d)}$, while the red dashed curves label the corresponding corrected frequencies $\omega_\beta^{(cr)} (= \omega_\beta^{(d)} + \Delta\omega_\beta)$, and the insert figures show the frequency shifts $\Delta\omega_\beta$. The effective qubit-qubit coupling strengths $g_{xy}^{(d)}$ (black solid curve) and $g_{xy}^{(cr)}$ (red dashed curve) are plotted via (c) node phase ϕ_y and (d) transition frequency ω_y. Here, $\omega_x/2\pi = 4.56$ GHz and $g_{xy}/2\pi = 1$ MHz; the other parameters are the same as in Fig. 2.

The transition frequency of qubit **x** in a decoupled coordinate is plotted in Fig. 4(a) ; the deviation between $\omega_x^{(cr)}$ and $\omega_x^{(d)}$ is larger in the regimes far from the zero magnetic flux points, which coincides with the curve of $\Delta\omega_x$ in the insert figure. On the contrary, the maximal deviation between $\omega_y^{(cr)}$ and $\omega_y^{(d)}$ appears at the regime close to the zero magnetic flux ($\Phi_{e,y} \to 0$ or $\phi_y \to 0$) in Fig. 4(b), which also coincides with the curve of $\Delta\omega_y$ in the insert figure.

If we replace the $\omega_\beta^{(d)}$ with $\omega_\beta^{(cr)}$ in Eq. (11), we can get the corrected effective qubit-qubit coupling $g_{xy}^{(cr)}$. The resonators' resonant frequencies ω_a and ω_b are fixed in this article, so the effective qubit-qubit couplings are mainly tuned by the qubits' transition frequencies ω_x and ω_y. By setting $\omega_x/(2\pi) = 4.56$ GHz, we plot the curves of effective qubit-qubit coupling $g_{xy}^{(cr)}$ and $g_{xy}^{(d)}$ on the respective ϕ_y and ω_y in Figs. 4(c) and 4(d), and the points satisfying $g_{xy}^{(cr)}/(2\pi) = 0$ Hz or $g_{xy}^{(d)}/(2\pi) = 0$ Hz correspond to the switching off position for the qubit-qubit interaction. The zero-value points of $g_{xy}^{(cr)}$ and $g_{xy}^{(cr)}$ are different, which reflects the effects of the nonlinear term H_{nl} (also the second excited state of a superconducting artificial atom) on the switching off positions. The calculation results of the corrections to qubit frequencies and effective qubit-qubit coupling strength can help to accurately design the superconducting quantum chip.

D. Switching off the qubit-qubit coupling

In this section, we study the effects of direct qubit-qubit coupling g_{xy} and qubit anharmonicity α_β on the effective qubit-qubit coupling $g_{xy}^{(cr)}$ and the switching off position. If we

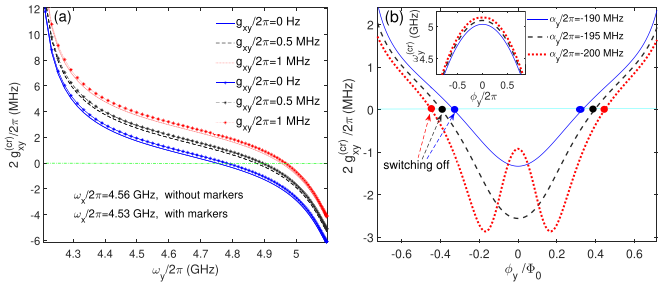

FIG. 5. Switching off the interaction between two qubits. The effects of (a) direct qubit-qubit coupling strengths and (b) qubit anharmonicities on the switching off positions. (a) The three types of line styles correspond to different direct qubit-qubit coupling strengths: (1) $g_{xy}/2\pi = 0$ Hz for blue solid curves, (2) $g_{xy}/2\pi = 0.5$ MHz for black dashed curves, and (3) $g_{xy}/2\pi = 1$ MHz for red dotted curves. For the curves without markers, $\omega_x/2\pi = 4.56$ GHz, while $\omega_x/2\pi = 4.53$ GHz for the curves with star markers. (b) The three curves correspond to different anharmonicities: (1) $\alpha_y/2\pi = -190$ MHz for the blue solid curve, (2) $\alpha_y/2\pi = -195$ MHz for the black dashed curve, and (3) $\alpha_y/2\pi = -200$ MHz for the red dotted curve. The variation of ω_y on the node phase ϕ_y is shown in the insert figure. We choose $\omega_x/2\pi = 4.56$ GHz and $g_{xy}/2\pi = 0.5$ MHz in (b). The other parameters of (a) and (b) are the same as in Fig. 2.

take the parameters of Fig. 2, we can get $g_{by}/\min(|\Delta_{by}|) \sim 1/3$ and $g_{ax}/\min(|\Delta_{ax}|) \sim 1/15$ in the idling states of qubits (without external magnetic field), so the qubits and resonators are in the dispersive or weak-dispersive coupling regimes. To see more clearly the working mechanism of switching off processes in the double-resonator couplers circuit, we plot the one-dimensional curves of effective qubit-qubit coupling $g_{xy}^{(cr)}$ with the variation of qubit transition frequency ω_y in Fig. 5(a). By fixing $\omega_x/(2\pi) = 4.56$ GHz, the three curves without markers in Fig. 5(a) correspond to different direct qubit-qubit coupling strengths: $g_{xy}/(2\pi) = 0$ Hz in the blue solid curve, $g_{xy}/(2\pi) = 0.5$ MHz in the black dashed curve, and $g_{xy}/(2\pi) = 1$ MHz in the red dotted curve. The crossing points of three curves with the zero-value line [$g_{xy}^{(cr)}/(2\pi) = 0$ Hz] are different, which means that the direct qubit-qubit coupling could affect the switching off positions. If we set $\omega_x/(2\pi) = 4.53$ GHz, the switching off points in the three marked curves show considerable shifts relative to the corresponding color curves without markers.

In Fig. 5(b), we plot the curves of effective qubit-qubit coupling $g_{xy}^{(cr)}$ on the node phase ϕ_y with $\omega_x/(2\pi) = 4.56$ GHz. For the same ranges of node phase ϕ_y, the qubit's maximal frequencies $\omega_y^{(\max)}$ are not the same for different anharmonicities α_y as shown in the insert figure. For different anharmonicities α_y, the shifts of switching off positions on three curves reflect the effects of the superconducting artificial atom's second excited states.

The frequency of qubit **y** should be tuned close to $\omega_y \approx \omega_x$ for the iSWAP gate and $\omega_y + \alpha_y \approx \omega_x$ for the controlled-Z gate. For the single-path coupler circuit, the switching off point is usually close to the idling coupler frequency (usually about 6.0 GHz), which is far from the two-qubit gate regimes (usually below 5.0 GHz). In the double-resonator couplers circuit, the switching off positions can be very close to the two-qubit gate regimes as shown in Fig. 5(a). So the maximal frequencies of couplers can be smaller in the double-resonator couplers superconducting circuit, which leaves wider available ranges for readout resonators (or qubits) and might relieve the frequency crowding on the superconducting quantum chip.

IV. STATIC ZZ COUPLING

The tunable coupler could isolate the qubits from surrounding environments for local quantum operations and reduce the accumulated phases for the quantum state preparations, and this can greatly enhance the fidelity of the two-qubit gate [4,9–15]. Because of the small anharmonicity of the Xmon qubit and the high-order quantum state exchanges (originating from the qubit-qubit and qubit-coupler interactions), the quantum state leakages and the parasitic crosstalks are still important obstructions for further enhancing the fidelity of the two-qubit gate [16]. Suppressing the residual coupling and the parasitic crosstalk among neighboring qubits are the leading tasks for enhancing the quality of the superconducting quantum chip [17,22,33–35].

The residual ZZ coupling consists of the static type ZZ coupling and the dynamic type ZZ coupling, but the dynamic ZZ coupling is usually suppressed by optimizing the microwave pulse shapes, which is not the interest of this article [16,34]. In this section, we mainly focus on the static ZZ coupling, which can be mitigated by the designing structures and working parameters of qubits and tunable couplers [12,17,22–24,33–38]. In the double-coupler superconducting quantum circuit, the direct qubit-qubit coupling can be arbitrarily small in principle, and this should be helpful for suppressing the static ZZ coupling. Also, the destructive interferences between double-path couplers might eliminate the static ZZ coupling [12,22–24].

A. Analytic calculations

In Figs. 2(a) and 2(b), we have numerically calculated the energy-level curves of states $|0100\rangle$, $|0010\rangle$, and $|0110\rangle$, and in principle the static ZZ coupling can be easily calculated through the definition $\xi_{ZZ} = \omega_{|0110\rangle} - \omega_{|0100\rangle} - \omega_{|0010\rangle} + \omega_{|0000\rangle}$. Practically, it is difficult to accurately fit the energy-level curves of qubits because the avoided crossing gaps are affected by multibody interactions. By setting $\omega_x/(2\pi) = 4.56$ GHz, if we tune the frequency of qubit **y** to be nearly resonant with qubit **x** ($\omega_y \approx \omega_x$), then we can get $g_{by}/|\Delta_{by}| \approx g_{bx}/|\Delta_{bx}| \sim 1/20$ and $g_{ax}/|\Delta_{ax}| \approx g_{ay}/|\Delta_{ay}| \sim 1/15$. Thus, the qubit-resonator regimes are dispersive coupling regimes, and the perturbation method can be used to analyze the static ZZ coupling close to the two-qubit gate regimes.

For convenience and consistency, we still use ω_β to describe the energy levels of the first excited state of qubit β in this section, and the energy level for the second excited state is $2\omega_\beta + \alpha_\beta$, where α_β is the qubit's anharmonicity. If we temporarily disregard the weak direct qubit-qubit and direct resonator-resonator interactions, up to the fourth-order perturbation theory the effective Hamiltonian on the qubits'

eigenstates space can be obtained as [31,32]

$$
\begin{aligned}
H'_m/\hbar = & \sum_{\lambda=a,b} \omega_\lambda c_\lambda^\dagger c_\lambda \\
& + \sum_{\beta=x,y} \sum_{\substack{\lambda=a,b \\ j_\beta=0,1,2,\ldots}} (\omega_{j_\beta} + \kappa_{\lambda,j_\beta} + \chi_{\lambda,j_\beta} c_\lambda^\dagger c_\lambda) |j_\beta\rangle\langle j_\beta| \\
& + \sum_{\beta=x,y} \sum_{j_\beta=0,1,2,\ldots} \Bigg[\sum_{\lambda=a,b} \mu_{\lambda,j_\beta} (c_\lambda^\dagger c_\lambda)^2 \\
& + \nu_{ab,j_\beta} c_a^\dagger c_a c_b^\dagger c_b + \nu_{ba,j_\beta} c_b^\dagger c_b c_a^\dagger c_a \Bigg] |j_\beta\rangle\langle j_\beta|. \qquad (15)
\end{aligned}
$$

The ket vector $|j_\beta\rangle$ describes the j_βth excited state of qubit β, with $j_\beta, j'_\beta = 0, 1, 2, \ldots$. We define $g_\lambda^{j_\beta j'_\beta}$ as the coupling strength between resonator λ and the transition $|j_\beta\rangle \leftrightarrow |j'_\beta\rangle$ of qubit β. Considering the selection rule, resonator λ can only interact with the neighboring quantum states of qubit β: $g_\lambda^{j_\beta j'_\beta} = 0$ for $j'_\beta \neq j_\beta \pm 1$. In this section, we neglect the small differences for the coupling strengths between resonator λ and different neighboring state transitions of qubit β, then $g_\lambda^{j_\beta-1,j_\beta} = g_\lambda^{j_\beta,j_\beta+1} = g_{\lambda\beta}(j_\beta = 1, 2, \ldots)$. Defining $\chi_\lambda^{j_\beta-1,j_\beta} = j_\beta g_{\lambda\beta}/[\Delta_{\lambda\beta} + (j_\beta - 1)\alpha_\beta]$, then $\kappa_{\lambda,j_\beta} = \chi_\lambda^{j_\beta-1,j_\beta}$ describes the level shifts of Lamb type for the quantum state $|j_\beta\rangle$ which is induced by the interaction between resonator λ and qubit $\beta(|j_\beta - 1\rangle \leftrightarrow |j_\beta\rangle$ and $|j_\beta\rangle \leftrightarrow |j_\beta + 1\rangle)$, while $\chi_{\lambda,j_\beta} = \chi_\lambda^{j_\beta-1,j_\beta} - \chi_\lambda^{j_\beta,j_\beta+1}$ describes the corresponding AC-Stark type dispersive shifts for the quantum state $|j_\beta\rangle$ [$\chi_{\lambda,0_\beta} = -\chi_\lambda^{0_\beta,1_\beta} = -g_{\lambda\beta}^2/(2\Delta_{\lambda\beta})$] [31,32]. If we add the contributions of second excited states of superconducting artificial atoms, besides the self-Kerr resonant term $\mu_{\lambda,j_\beta}(c_\lambda^\dagger c_\lambda)^2$, the cross-Kerr resonant terms $\nu_{ab,j_\beta} c_a^\dagger c_a c_b^\dagger c_b$ and $\nu_{ba,j_\beta} c_b^\dagger c_b c_a^\dagger c_a$ should also make contributions to the static ZZ coupling (as will be discussed in the following sections) [31,32,39].

If we temporarily disregard the cross-Kerr resonant terms, after adding the contributions of weak direct qubit-qubit coupling, then the static ZZ coupling in qubit-resonator dispersive coupling regimes can be obtained as [8,16,17,24]

$$
\xi_{ZZ}^{(2)} = \frac{2(g_{xy})^2(\alpha_x + \alpha_y)}{(\Delta_{xy} + \alpha_y)(\Delta_{xy} - \alpha_x)}, \qquad (16)
$$

$$
\begin{aligned}
\xi_{ZZ,\lambda}^{(3)} = & 2g_{xy}g_{\lambda x}g_{\lambda y}\Bigg[\frac{1}{\Delta_{\lambda y}}\left(\frac{1}{\Delta_{xy}} - \frac{2}{\Delta_{xy} + \alpha_y}\right) \\
& - \frac{1}{\Delta_{\lambda y}}\left(\frac{1}{\Delta_{xy}} - \frac{2}{\Delta_{xy} - \alpha_x}\right)\Bigg], \qquad (17)
\end{aligned}
$$

$$
\begin{aligned}
\xi_{ZZ,\lambda}^{(4s)} = & \frac{2(g_{\lambda y})^2(g_{\lambda x})^2}{\Delta_{\lambda y} + \Delta_{\lambda x} - \alpha_\lambda}\left(\frac{1}{\Delta_{\lambda y}} + \frac{1}{\Delta_{\lambda x}}\right)^2 \\
& - \frac{(g_{\lambda y})^2(g_{\lambda x})^2}{\Delta_{\lambda y}^2}\left(\frac{1}{\Delta_{xy}} + \frac{1}{\Delta_{\lambda x}} - \frac{2}{\Delta_{xy} - \alpha_x}\right) \\
& - \frac{(g_{\lambda y})^2(g_{\lambda x})^2}{\Delta_{\lambda x}^2}\left(\frac{2}{\Delta_{xy} + \alpha_y} - \frac{1}{\Delta_{xy}} + \frac{1}{\Delta_{\lambda y}}\right). \qquad (18)
\end{aligned}
$$

The $\xi_{ZZ}^{(2)}$ is the second-order static ZZ coupling between two qubits, and $\xi_{ZZ,\lambda}^{(3)}$ describes the third-order static ZZ coupling between two qubits intermediated by resonator λ. We use $\xi_{ZZ,\lambda}^{(4s)}$ to label fourth-order static ZZ coupling contributed by the self-Kerr resonance intermediated by resonator λ, and $\xi_{ZZ,\lambda}^{(4c)}$ describes the static ZZ coupling induced by the cross-Kerr resonance.

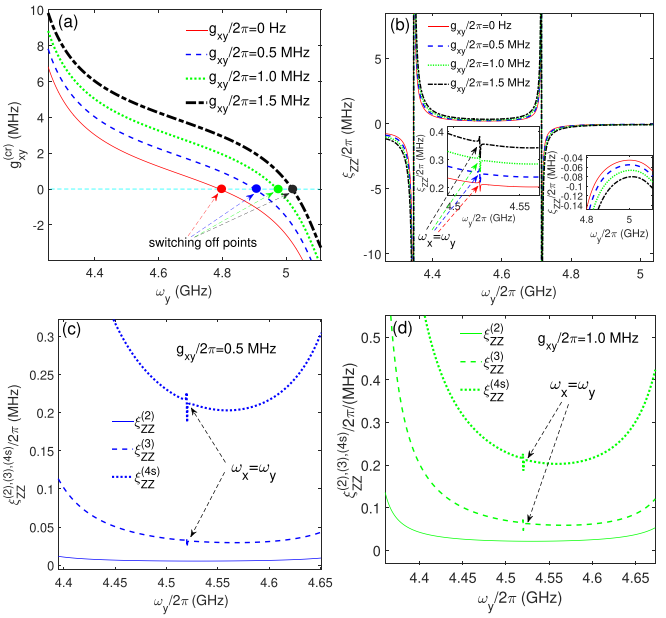

FIG. 6. Suppression of static ZZ coupling. The (a) effective qubit-qubit coupling and (b) static ZZ coupling are plotted for different direct qubit-qubit coupling strengths: (1) $g_{xy}/2\pi = 0$ Hz (red solid curve), (2) $g_{xy}/2\pi = 0.5$ MHz (blue dashed curve), (3) $g_{xy}/2\pi = 1$ MHz (green dotted curve), and (4) $g_{xy}/2\pi = 1.5$ MHz (black dashed-dot curve). The insert figures are the partial enlarged drawing. The $\xi_{ZZ}^{(2)}$, $\xi_{ZZ}^{(3)}(=\sum_{\lambda=a,b}\xi_{ZZ,\lambda}^{(3)})$, and $\xi_{ZZ}^{(4s)}(=\sum_{\lambda=a,b}\xi_{ZZ,\lambda}^{(4s)})$ are plotted in (c) and (d), and they respectively take the parameters of the blue dashed and black dashed-dot curves in (b). The frequency of qubit **x** is fixed at $\omega_x/2\pi = 4.52$ GHz, and the other parameters of (a)–(d) are the same as in Fig. 2.

Even being listed together, the second-order $\xi_{ZZ}^{(2)}$, third-order $\xi_{ZZ}^{(3)} = \sum_{\lambda=a,b}\xi_{ZZ,\lambda}^{(3)}$, and fourth-order (self-Kerr) $\xi_{ZZ}^{(4s)} = \sum_{\lambda=a,b}\xi_{ZZ,\lambda}^{(4s)}$ static ZZ coupling terms come from different sources. As shown in Eqs. (16) and (17), the second-order term $\xi_{ZZ}^{(2)}$ originates from the direct qubit-qubit coupling [6–8,17] and the fourth-order term $\xi_{ZZ}^{(4s)}$ results from the perturbation expansion of qubit-resonator dispersive coupling [31,39], while the third-order term $\xi_{ZZ}^{(3)}$ is joint effects of direct qubit-qubit coupling and qubit-resonator interaction. Here, $\alpha_\lambda = \sum_{\beta=x,y}\alpha_\beta(g_{\lambda\beta}/\Delta_{\lambda\beta})^4$ describes the nonlinearity of resonator λ induced by the qubit-resonator dispersive coupling [32]. Since $g_{xy}, g_{ab} \ll g_{\lambda\beta}$, the contributions of direct qubit-qubit and resonator-resonator couplings to fourth-order static ZZ coupling are neglected.

B. Suppression of the static ZZ coupling

In this section, we try to suppress the static ZZ coupling with direct qubit-qubit coupling, which can be arbitrarily small in the double-coupler superconducting circuit. By setting $\omega_x/(2\pi) = 4.52$ GHz, the curves of static ZZ coupling $\xi_{ZZ} = \xi_{ZZ}^{(2)} + \xi_{ZZ}^{(3)} + \xi_{ZZ}^{(4s)}$ are plotted in Fig. 6(b) according

to Eqs. (16)–(18). The four curves correspond to different direct qubit-qubit coupling strengths. In the regimes suitable for the two-qubit gates, the values of static ZZ coupling are apparently suppressed by the weaker direct qubit-qubit coupling as shown in the insert figure. And, the values of $\xi_{ZZ}^{(3)}$ and $\xi_{ZZ}^{(4s)}$ are obviously suppressed by weaker direct qubit-qubit coupling in Fig. 6(c) [$g_{xy}/(2\pi) = 0.5$ MHz] compared with the results in Fig. 6(d) [$g_{xy}/(2\pi) = 1.0$ MHz]. As shown in Figs. 6(b)–6(f), the static ZZ coupling can be suppressed below sub-MHz in a double-resonator coupler circuit, which is on a similar level with the transmon-based coupler circuit [7,16].

For each static ZZ coupling curve in Fig. 6(b), two poles appear at $\Delta_{xy} = \alpha_x$ and $\Delta_{xy} = -\alpha_y$ which originate from resonant state exchanges between the state $|0200\rangle \leftrightarrow |0110\rangle$ and $|0020\rangle \leftrightarrow |0110\rangle$, respectively. There is also a pole located at $\omega_y = \omega_x$ in each curve of static ZZ coupling in Fig. 6(b), and the pole also appears in the dashed curves (third-order static ZZ coupling) and dotted curve (fourth-order self-Kerr resonance static ZZ coupling) in Figs. 6(c) and 6(d), so it should originate the qubit-qubit resonance state exchanges as indicated by the term $1/\Delta_{xy}$ contained in Eqs. (17) and (18). As shown in Fig. 6(a), the switching off positions in the double-resonator couplers circuit can be below 5 GHz, which is very close to the regimes of a two-qubit gate. If the frequency of qubit **y** is tuned away from the switching off positions, the effective qubit-qubit coupling quickly increases to above 5 MHz for the two-qubit gates.

C. Cancellation of the static ZZ coupling

The nonzero residual coupling leads to unnecessary always-on quantum gates and additional accumulated phases, which are the dominant obstructions for the further enhancement of two-qubit gate fidelities. Recently, some work announced the elimination of the static ZZ coupling in the superconducting quantum chip [24,35,36], and it might also be removed in our proposed scheme through the destructive interference of double-path couplers.

When we tune frequencies of qubit **x** to satisfy $\omega_x < \omega_a$, the static ZZ coupling ξ_{ZZ} can be zero at some points as shown in Figs. 7(b) and 7(d), thus the static ZZ coupling is eliminated in the double-resonator coupler circuit. The signs of second-order $\xi_{ZZ}^{(2)}$, third-order $\xi_{ZZ}^{(3)}$, and fourth-order $\xi_{ZZ}^{(4s)}$ (self-Kerr resonance) static ZZ coupling are different in Figs. 7(e) and 7(f), and they cancel each other and eliminate the static ZZ coupling at certain points. It should be mentioned that the poles at $\omega_y = \omega_x$ in Fig. 6 do not appear in Fig. 7(b) just because they are outside the scope of the drawing.

As shown in Figs. 7(a) and 7(b), the static ZZ coupling is not switched off together with the effective qubit-qubit coupling. This result is not difficult to understand for the perturbation calculation methods [16,24], because the effective qubit-qubit coupling is calculated only up to the second-order dispersive interaction (AC-Stark/Lamb shifts), but static ZZ coupling contains some high-order effects, such as self-Kerr resonance, cross-Kerr resonance, highly excited state corrections, and so on. The intervals between zero-value positions of static ZZ coupling and effective qubit-qubit coupling change for different direct qubit-qubit coupling strengths, and the black dash-dotted curves [$g_{xy}/(2\pi) = 1.6$ MHz] have

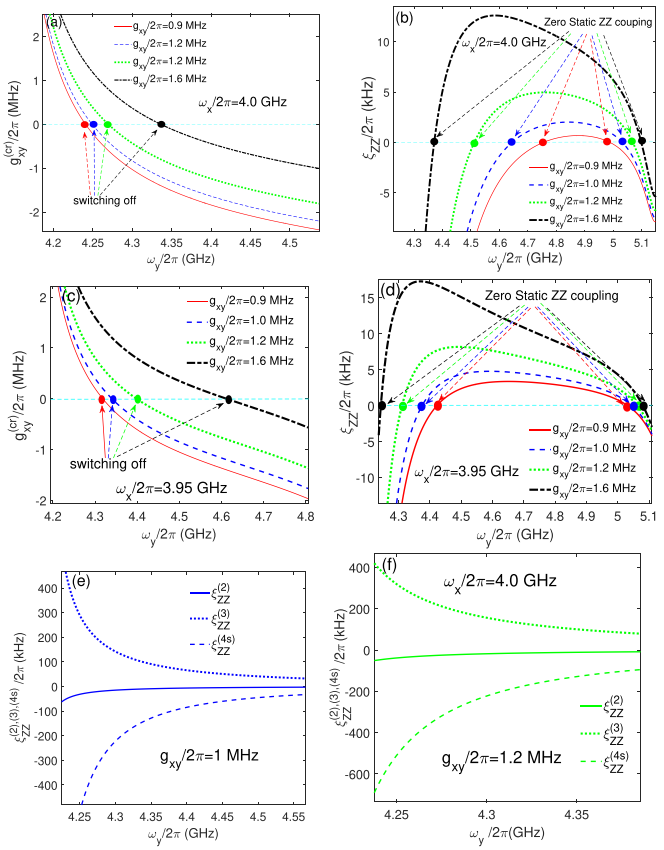

FIG. 7. Cancellation of static ZZ coupling. The effective qubit-qubit coupling and the static ZZ coupling are respectively plotted in (a) and (b) in the case of $\omega_x/2\pi = 4.0$ GHz, and the corresponding results for $\omega_x/2\pi = 3.95$ GHz are shown in (c) and (d). The four curves in each figure of (a)–(d) correspond to different direct qubit-qubit coupling strengths: (1) $g_{xy}/2\pi = 0.9$ MHz (red solid curves), (2) $g_{xy}/2\pi = 1.0$ MHz (blue dashed curves), (3) $g_{xy}/2\pi = 1.2$ MHz (green dotted curves), and (4) $g_{xy}/2\pi = 1.6$ MHz (black dash-dotted curves). The $\xi_{ZZ}^{(2)}$, $\xi_{ZZ}^{(3)}$, and $\xi_{ZZ}^{(4s)}$ are plotted in (e) and (f), and they respectively take the parameters of the blue dashed and green dotted curves of (b). The other parameters of (a)–(f) are the same as in Fig. 2.

the smallest interval in Figs. 7(a) and 7(b). When we set $\omega_x/(2\pi) = 3.95$ GHz, the blue dashed curves [$g_{xy}/(2\pi) = 1.0$ MHz] get the smallest interval in Figs. 7(c) and 7(d). So, the interval between the switching off and zero static ZZ coupling points can be tuned by direct qubit-qubit coupling and the frequencies of qubits, and it is possible to conduct the switching off and two-qubit gates at both the zero static ZZ coupling regimes in the double-coupler superconducting circuit.

D. Corrections to static ZZ coupling

If we incorporate the variations of nonlinear term $(\alpha_\beta/2)a_\beta^\dagger a_\beta^\dagger a_\beta a_\beta$ during the decoupling processes of the qubit-resonator interactions, then the cross-Kerr resonances will contribute to the ZZ coupling [31,32,39]. The resonator couplers are not pumped by external fields, and the average cavity photon number is much smaller than one, so

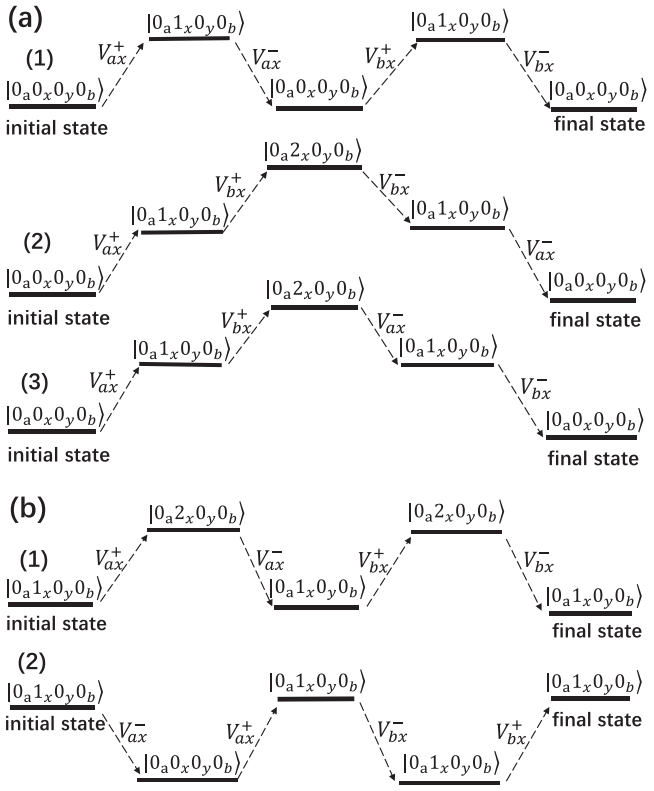

FIG. 8. Energy-level diagrams of cross-Kerr resonances. The virtual photon exchange among qubit **x**, resonator **a**, and resonator **b** with qubit **x** initially in (a) the ground state and (b) the first excited state. $V_{\lambda x}^{-}$ (or $V_{\lambda x}^{+}$) describes the virtual photon annihilation (or creation) process through the interaction between qubit **x** and resonator λ, and $V_{\lambda x}^{-} = (V_{\lambda x}^{+})^{\dagger}$. The energy-level diagram of cross-Kerr resonances for qubit **y** can be obtained by replacing qubit **x** with qubit **y**.

the single virtual photon exchanges will dominate the cross-Kerr resonance processes. The cross-Kerr resonance terms $\nu_{ab,j_\beta} c_a^{\dagger} c_a c_b^{\dagger} c_b$ and $\nu_{ba,j_\beta} c_b^{\dagger} c_b c_a^{\dagger} c_a$ in Eq. (15) describe the physical processes of virtual photon exchange between a qubit and two resonators, and we plot the energy-level diagrams of the single-virtual photon exchange process of cross-Kerr resonance for qubit **x** in Fig. 8. For simplicity, only the three lowest energy levels of superconducting artificial atoms are considered. The virtual photon exchange processes of cross-Kerr resonance for qubit **y** can be obtained by replacing the **x** with **y** in Fig. 8.

When qubit **x** is initially in the ground state, the energy-level diagrams of cross-Kerr resonance among qubit **x**, resonator **a**, and resonator **b** are shown in Fig. 8(a). The six cross-Kerr resonances are attributed as three types of virtual photon exchange processes among qubit **x**, resonator **a**, and resonator **b** [31]. In the first type, qubit **x** absorbs a virtual photon from resonator **a** (or **b**) and transits to the first excited states from the ground state, and it immediately returns the virtual photon to resonator **a** (or **b**) and decays to the ground state. Subsequently, qubit **x** jumps to the first excited state again by getting another virtual photon from resonator **b** (or **a**), and finally it emits the virtual photon to resonator **b** (or **a**) and decays to the ground state. In the second type, qubit **x** transits to the first excited state from the ground state by absorbing a virtual photon from resonator **a** (or **b**) and immediately jumps to the second excited state by taking another virtual photon from resonator **b** (or **a**). Subsequently, the qubit jumps to the first excited state by emitting a virtual photon to resonator **b** (or **a**), and finally decays to the ground state by emitting another virtual photon to resonator **a** (or **b**). In the third type, the first two transition processes are the same as the second type, but the qubit first returns a virtual photon to resonator **a** (or **b**) in the third transition process and transits to the first excited state, and finally decays to the ground state by emitting another photon to resonator **b** (or **a**). The virtual photon exchange processes for cross-Kerr resonances among qubit **y**, resonator **a**, and resonator **b** can be obtained by replacing qubit **x** with qubit **y** in Fig. 8(a). Adding together the contributions of the six types of cross-Kerr resonant processes, we can obtain the energy-level corrections to the ground state of qubit β [31],

$$\xi_{ZZ,\beta}^{(4c,0)}|0_\beta\rangle\langle 0_\beta| = g_{a\beta}^2 g_{b\beta}^2\left[\frac{2}{\Delta_{a\beta}\Delta_{b\beta}\omega_\beta}+\frac{1}{2\omega_\beta+\alpha_\beta-\omega_a-\omega_b}\times\left(\frac{2\omega_\beta-\omega_a-\omega_b}{\Delta_{a\beta}\Delta_{b\beta}}\right)^2\right]|0_\beta\rangle\langle 0_\beta|. \quad (19)$$

For simplicity, we have neglected the small differences in the interactions of a resonator with different energy levels of superconducting artificial atom, that is, $g_\lambda^{j_\beta,j'_\beta} = g_{\lambda\beta}$.

When qubit **x** is initially in the first excited state, the energy-level diagrams of cross-Kerr resonance among qubit **x**, resonator **a**, and resonator **b** are shown in Fig. 8(b). The four cross-Kerr resonances are attributed as two types of virtual photon exchange processes. In the first type, qubit **x** in the first excited state absorbs a virtual photon from resonator **a** (or **b**) and transits to the second excited state, and it immediately returns the photon to resonator **a** (or **b**) and jumps to the first excited state. Subsequently, the qubit jumps to the second excited state again by getting another virtual photon from resonator **b** (or **a**), and finally it emits the photon to resonator **b** (or **a**) and jumps to the first excited state. In the second type, qubit **x** (in the first excited state) emits a virtual photon to resonator **a** (or **b**) and decays to the ground state, then immediately transits to the first excited state by absorbing a virtual photon from resonator **a** (or **b**). Subsequently, the qubit emits a virtual photon to resonator **b** (or **a**) and decays to the ground state, then immediately absorbs another virtual photon from resonator **b** (or **a**), and finally jumps to the first excited state. The virtual photon exchange processes for cross-Kerr resonances among qubit **y**, resonator **a**, and resonator **b** can be obtained by replacing qubit **x** with qubit **y** in Fig. 8(b). Adding together the contributions of the four types of cross-Kerr resonant processes, we can obtain the energy-level corrections to the first excited state of qubit β [31],

$$\xi_{ZZ,\beta}^{(4c,1)}|1_\beta\rangle\langle 1_\beta| = \frac{2g_{a\beta}^2 g_{b\beta}^2}{\omega_\beta(\Delta_{a\beta}+\alpha_\beta)(\Delta_{b\beta}+\alpha_\beta)}|1_\beta\rangle\langle 1_\beta| + \frac{2g_{a\beta}^2 g_{b\beta}^2}{\omega_\beta\Delta_{a\beta}\Delta_{b\beta}}|1_\beta\rangle\langle 1_\beta|. \quad (20)$$

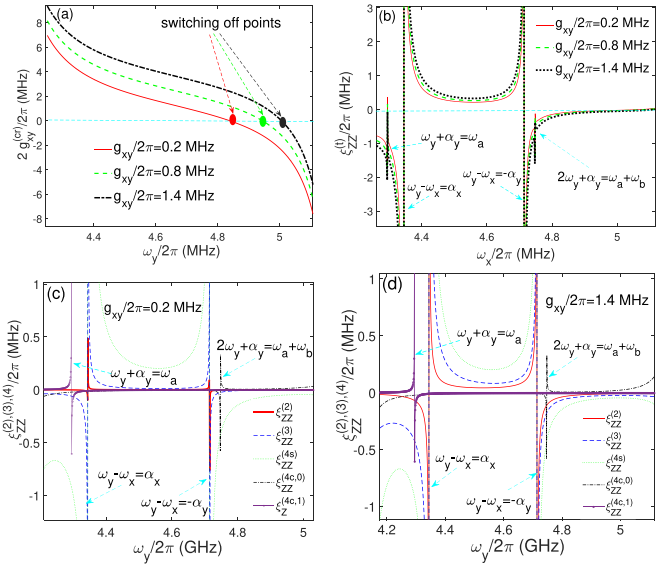

FIG. 9. The static ZZ coupling corrected by the cross-Kerr resonances. We plot (a) the effective qubit-qubit coupling and (b) the static ZZ coupling $\xi_{ZZ}^{(t)}=\xi_{ZZ}^{(2)}+\xi_{ZZ}^{(3)}+\xi_{ZZ}^{(4s)}+\xi_{ZZ}^{(4c,0)}-\xi_{ZZ}^{(4c,1)}$ at different direct qubit-qubit coupling strengths: (1) $g_{xy}/2\pi=0.2$ MHz (red solid curve), (2) $g_{xy}/2\pi=1.4$ MHz (green dashed curve), and (3) $g_{xy}/2\pi=2$ MHz (black dotted curve). $\xi_{ZZ}^{(2)}$ (red solid curve), $\xi_{ZZ}^{(3)}=\sum_{\lambda=a,b}\xi_{ZZ,\lambda}^{(3)}$ (blue dashed curve), $\xi_{ZZ}^{(4s)}=\sum_{\lambda=a,b}\xi_{ZZ,\lambda}^{(4s)}$ (green dotted curve), $\xi_{ZZ}^{(4c,0)}=\sum_{\beta=x,y}\xi_{ZZ,\beta}^{(4c,0)}$ (black dashed-dot curve), and $\xi_{ZZ}^{(4c,1)}=\sum_{\beta=x,y}\xi_{ZZ,\beta}^{(4c,1)}$ (marked purple solid curve) are plotted with (c) $g_{xy}/2\pi=0.2$ MHz and (d) $g_{xy}/2\pi=1.4$ MHz. The parameters of the four figures are the same as in Fig. 2 except for $\omega_x/2\pi=4.52$ GHz.

Adding the corrections by the cross-Kerr resonances, the total ZZ coupling can be defined as $\xi_{ZZ}^{(t)}=\xi_{ZZ}^{(2)}+\xi_{ZZ}^{(3)}+\xi_{ZZ}^{(4s)}+\xi_{ZZ}^{(4c,0)}-\xi_{ZZ}^{(4c,1)}$, with $\xi_{ZZ}^{(3)}=\sum_{\lambda=a,b}\xi_{ZZ,\lambda}^{(3)}$, $\xi_{ZZ}^{(4s)}=\sum_{\lambda=a,b}\xi_{ZZ,\lambda}^{(4s)}$, $\xi_{ZZ}^{(4c,0)}=\sum_{\beta=x,y}\xi_{ZZ,\beta}^{(4c,0)}$, and $\xi_{ZZ}^{(4c,1)}=\sum_{\beta=x,y}\xi_{ZZ,\beta}^{(4c,1)}$. We plot the second-order $\xi_{ZZ}^{(2)}$ (red solid curves), third-order $\xi_{ZZ}^{(3)}$ (blue dashed curves), and fourth-order (self-Kerr resonance) $\xi_{ZZ}^{(4s)}$ (green dotted curves) static ZZ coupling in Fig. 9(c) $[g_{xy}/(2\pi)=0.2$ MHz] and Fig. 9(d) $[g_{xy}/(2\pi)=1.4$ MHz]. By reducing the direct qubit-qubit coupling strengths, the values of static ZZ coupling curves are apparently suppressed in Fig. 9(c) $[g_{xy}/(2\pi)=0.2$ MHz] compared with the result in Fig. 9(d) $[g_{xy}/(2\pi)=1.4$ MHz]. The energy-level corrections to the qubit's ground state ($\xi_{ZZ}^{(4c,0)}$) and first excited state ($\xi_{ZZ}^{(4c,1)}$) by the cross-Kerr resonances are respectively plotted in the black dashed-dot curves and marked purple solid curves in Figs. 9(c) and 9(d).

The curves of effective qubit-qubit coupling are plotted in Fig. 9(a), and values of direct qubit-qubit coupling affect switching off positions. Similar to Fig. 6(b), the two poles located at $\Delta_{xy}=\alpha_x$ and $\Delta_{xy}=-\alpha_y$ also appear in each curve of static ZZ coupling $\xi_{ZZ}^{(t)}$ in Fig. 9(b). But, there are two new poles in each curve of static ZZ coupling $\xi_{ZZ}^{(t)}$ in Fig. 9(b) which should originate from the cross-Kerr resonance [31,32]. As indicated by Eqs. (19) and (20), the cross-Kerr resonances through virtual photon exchanges induce additional poles for the static ZZ coupling at the point: $2\omega_\beta+\alpha_\beta=\omega_a+\omega_b$ [from Eq. (19)], $\omega_\beta+\alpha_\beta=\omega_a$ [from Eq. (20)], and $\omega_\beta+\alpha_\beta=\omega_b$ [from Eq. (20)]. So, we can see two new poles at $\omega_y+\alpha_y=\omega_a$ and $2\omega_y+\alpha_y=\omega_a+\omega_b$ in each curve of Fig. 9(b). Another pole ($\omega_y+\alpha_y=\omega_b$) is out of the scope of the drawing. As shown in Figs. 9(c) and 9(d), the pole at $2\omega_y+\alpha_y=\omega_a+\omega_b$ only appears on the black dash-dotted curves, which correspond to the level correction to qubits' ground states by the cross-Kerr resonance $\xi_{ZZ}^{(4c,0)}$, while the pole at $\omega_y+\alpha_y=\omega_a$ only appears in the marked purple solid curve, which describes the level correction to qubits' first excited states by the cross-Kerr resonance $\xi_{ZZ}^{(4c,1)}$. In this article, we neglect the level corrections of cross-Kerr resonances to the double-excited state $|01_x1_y0\rangle$, which should correspond to more complex physical processes.

V. CONCLUSIONS

In conclusion, we have studied the mechanism of the switching off in the superconducting circuit consisting of two fixed-frequency resonator couplers. The induced indirect qubit-qubit coupling by two resonators can be canceled, so the switching off can be realized without direct qubit-qubit coupling. The frequencies of couplers can be much smaller than the single transmon-based coupler circuit, and this leaves wider available frequency spaces for couplers (or qubits), thus the frequency crowding on the superconducting chip might be relieved.

Weak direct qubit-qubit coupling can be used to suppress the static ZZ coupling in the double-coupler circuit, and the destructive interferences between double-path couplers can eliminate the static ZZ coupling, thus the quality of the superconducting quantum chip might be enhanced. Our proposed double-resonator couplers scheme can unfreeze some restrictions on the superconducting quantum chip, mitigate the static ZZ coupling, and also save the dilution refrigerator lines, which might be a promising platform for the superconducting quantum chip.

ACKNOWLEDGMENTS

H.W. is supported by the Natural Science Foundation of Shandong Province under Grant No. ZR2023LZH002 and the Inspur artificial intelligence research institute. Y.J.Z. is supported by Beijing Natural Science Foundation under Grant No. 4222064 and NSFC under Grant No. 11904013. X.-W.X. is supported by the National Natural Science Foundation of China (Grants No. 12064010 and No. 12247105), the Science and Technology Innovation Program of Hunan Province (Grant No. 2022RC1203), Natural Science Foundation of Hunan Province of China (Grant No. 2021JJ20036), and Hunan provincial major sci-tech program (Grant No. 2023ZJ1010).

APPENDIX A: NUMERICAL CALCULATION OF ENERGY LEVELS

In this section, we use the numerical method to calculate the two-dimensional energy-level curved surfaces of the double-resonator couplers circuit (Fig. 1). Since the anhar-

monicities of the Xmon qubit are very small, we regard the superconducting artificial atom as a multi-energy-level system in this section [16,31]. The Hamiltonian for the circuit in Fig. 1 can be written as

$$\begin{aligned} H_m/\hbar = &\sum_{\lambda=a,b}\omega_\lambda c_\lambda^\dagger c_\lambda + \sum_{j_\beta}\omega_{j_\beta j'_\beta}J^z_{j_\beta j'_\beta} + g_{ab}(c_a^\dagger c_b + c_b^\dagger c_a) \\ &+ \sum_{\substack{\lambda=a,b;\beta=x,y \\ j_\beta, j'_\beta=0,1,2,\ldots}} g_\lambda^{j_\beta, j'_\beta}\left(J^+_{j'_\beta j_\beta} + J^-_{j_\beta j'_\beta}\right)(c_\lambda + c_\lambda^\dagger) \\ &+ \sum_{\substack{j_x, j'_x, j''_y, j'''_y \\ =0,1,2,\ldots}} g_{xy}^{j_x j'_x, j''_y j'''_y}\left(J^+_{j'_x j_x}J^-_{j''_y j'''_y} + J^+_{j'''_y j''_y}J^-_{j_x j'_x}\right), \end{aligned} \tag{A1}$$

where $j_\beta, j'_\beta, j''_\beta, j'''_\beta = 0, 1, 2, 3, \ldots$, and they respectively label the j_βth, j'_βth, j''_βth, and j'''_βth quantum states of qubit β, with $j'''_\beta > j''_\beta$ and $j'_\beta > j_\beta$. Between the quantum states $|j_\beta\rangle$ and $|j'_\beta\rangle$, we define the angular momentum operators as $\vec{J}_{j_\beta j'_\beta} = [J^x_{j_\beta j'_\beta}, J^y_{j_\beta j'_\beta}, J^z_{j_\beta j'_\beta}]$. The ladder operators can be introduced by $J^+_{j_\beta j'_\beta} = |j'_\beta\rangle\langle j_\beta|$ and $J^-_{j_\beta j'_\beta} = |j_\beta\rangle\langle j'_\beta|$, thus we can get $J^z_{j_\beta j'_\beta} = |j'_\beta\rangle\langle j'_\beta| - |j_\beta\rangle\langle j_\beta|$, $J^x_{j_\beta j'_\beta} = (J^+_{j_\beta j'_\beta} + J^-_{j_\beta j'_\beta})/2$, and $J^y_{j_\beta j'_\beta} = (J^+_{j_\beta j'_\beta} - J^-_{j_\beta j'_\beta})/(2i)$. The corresponding transition frequency between states $|j_\beta\rangle$ and $|j'_\beta\rangle$ is defined as $\omega_{j_\beta j'_\beta}$, and $g_\lambda^{j_\beta, j'_\beta}$ describes the corresponding coupling strengths with resonator coupler λ. $g_{xy}^{j_x j'_x, j''_y j'''_y}$ describes the direct coupling strengths between the transition processes of $|j'_x\rangle \leftrightarrow |j_x\rangle$ for qubit **x** and $|j'''_y\rangle \leftrightarrow |j''''_y\rangle$ for qubit **y**.

With the QUTIP software, we calculate the two-dimensional curved surfaces for the energy level of single-excited [Figs. 10(a)–10(d)] and double-excited [Figs. 10(e)–10(s)] states. During the numerical calculations with the QUTIP software, we truncate to the second excited states of qubits and assume $g_\lambda^{j_\beta, j'_\beta} = g_\lambda^{j'_\beta, j_\beta} = g_{\lambda\beta}$ and $g_{yx}^{j_x j'_x, j''_y j'''_y} = g_{xy}^{j'_y j_y, j'''_x j''_x} = g_{xy}$. Because of the anticrossing effects, each curved surface in Fig. 10 cannot describe a total energy level of a certain quantum state, and we label the z axis of each figure by the corresponding state at zero magnetic flux.

APPENDIX B: CIRCUIT QUANTIZATION

In this section, we conduct the quantization for the superconducting circuit in Fig. 1. The kinetic energy of the superconducting circuit can be obtained as [17,20]

$$\begin{aligned} T = &\tfrac{1}{2}\left(C_a\dot{\phi}_a^2 + C_b\dot{\phi}_b^2 + C_x\dot{\phi}_x^2 + C_y\dot{\phi}_y^2\right) \\ &+ \tfrac{1}{2}C_{ab}(\dot{\phi}_a - \dot{\phi}_b)^2 + \tfrac{1}{2}C_{xy}(\dot{\phi}_x - \dot{\phi}_y)^2 \\ &+ \tfrac{1}{2}C_{ax}(\dot{\phi}_a - \dot{\phi}_x)^2 + \tfrac{1}{2}C_{ay}(\dot{\phi}_a - \dot{\phi}_y)^2 \\ &+ \tfrac{1}{2}C_{bx}(\dot{\phi}_b - \dot{\phi}_x)^2 + \tfrac{1}{2}C_{by}(\dot{\phi}_b - \dot{\phi}_y)^2. \end{aligned} \tag{B1}$$

As indicated by Fig. 1(b), the self-capacitance of the qubits and resonators is C_η, and the relative capacitance between two arbitrary devices is defined as $C_{\eta\eta'}(C_{\eta\eta'} = C_{\eta'\eta})$, where $\eta, \eta' = a, b, x, y$ with $\eta \neq \eta'$. Here, ϕ_a and ϕ_b are the respective magnetic fluxes of the circuit nodes of resonators **a** and **b**, while ϕ_x and ϕ_y are the respective node fluxes of qubits **x** and **y**. If we define the vector $\vec{\phi} = [\phi_a, \phi_b, \phi_x, \phi_y]$, the kinetic energy in Eq. (B1) can be written as $T = \frac{1}{2}\dot{\vec{\phi}}^T C\dot{\vec{\phi}}$, with

$$C = \begin{pmatrix} C_{11} & -C_{ab} & -C_{ax} & -C_{ay} \\ -C_{ab} & C_{22} & -C_{bx} & -C_{by} \\ -C_{ax} & -C_{bx} & C_{33} & -C_{xy} \\ -C_{ay} & -C_{by} & -C_{xy} & C_{44}. \end{pmatrix}, \tag{B2}$$

where we have defined the coefficients: $C_{11} = C_a + C_{ab} + C_{ax} + C_{ay}$, $C_{22} = C_{ab} + C_b + C_{bx} + C_{by}$, $C_{33} = C_{ax} + C_{bx} + C_x + C_{xy}$, and $C_{44} = C_{ay} + C_{by} + C_{xy} + C_y$.

The potential energy for the superconducting circuit can be written as

$$\begin{aligned} U = &\frac{\phi_a^2}{2L_a} + \frac{\phi_b^2}{2L_b} + E_{J_x}\left[1 - \cos\left(\frac{2\pi}{\Phi_0}\phi_x\right)\right] \\ &+ E_{J_y}\left[1 - \cos\left(\frac{2\pi}{\Phi_0}\phi_y\right)\right], \end{aligned} \tag{B3}$$

where $E_{J_\beta} = I_{c\beta}\Phi_0/2\pi$ is the Josephson energy of qubit β, $I_{c\beta}$ is the corresponding critical current, and $\Phi_0 = h/2e$ is the flux quantum.

The Lagrangian of the superconducting circuit can be obtained by the definition $L = T - U$, thus the generalized momentum can be defined as $q_\eta = \partial L/\partial\dot{\phi}_\eta$ $(\eta = a, b, x, y)$, and it can be written in the vector form as $\vec{q} = [q_a, q_b, q_x, q_y]$. Thus, the Hamiltonian of the superconducting circuit can be written as $H = \vec{q}\cdot\dot{\vec{\phi}} - L = \frac{1}{2}\vec{q}^T C^{-1}\vec{q} + U$, and the inverse matrix is defined as

$$C^{-1} = \frac{A^*}{|C|} = \frac{1}{||C||}\begin{pmatrix} A_{11} & A_{21} & A_{31} & A_{41} \\ A_{12} & A_{22} & A_{32} & A_{42} \\ A_{13} & A_{23} & A_{33} & A_{43} \\ A_{14} & A_{24} & A_{34} & A_{44} \end{pmatrix}, \tag{B4}$$

where A^* is the adjugate matrix of A. With the conditions $C_{ab} \ll C_{xy} \ll C_{ax}, C_{ay}, C_{bx}, C_{by} \ll C_x, C_y \ll C_a, C_b$, thus $\|C\| \approx C_a C_b C_x C_y$, and we get approximate expressions for the elements in A^* as

$$\begin{aligned} A_{11} &= C_{22}\left(C_{33}C_{44} - C_{xy}^2\right) + C_{bx}(-C_{bx}C_{44} - C_{xy}C_{by}) \\ &\quad - C_{by}(C_{bx}C_{xy} + C_{33}C_{by}) \approx C_bC_xC_y, \\ A_{12} &= C_{ab}\left(C_{33}C_{44} - C_{xy}^2\right) - C_{bx}(-C_{ax}C_{44} - C_{xy}C_{ay}) \\ &\quad + C_{by}(C_{ax}C_{xy} + C_{33}C_{ay}) \\ &\approx C_{ab}C_xC_y + C_{ax}C_{bx}C_y + C_{ay}C_{by}C_x, \\ A_{13} &= C_{ab}(C_{bx}C_{44} + C_{by}C_{xy}) + C_{22}(C_{ax}C_{44} + C_{xy}C_{ay}) \\ &\quad - C_{by}(C_{ax}C_{by} - C_{bx}C_{ay}) \approx C_bC_yC_{ax}, \\ A_{14} &= C_{ab}(C_{bx}C_{xy} + C_{33}C_{by}) + C_{22}(C_{ax}c_{xy} + C_{33}C_{ay}) \\ &\quad + C_{bx}(C_{ax}C_{by} - C_{bx}C_{ay}) \approx C_bC_xC_{ay}, \\ A_{21} &= C_{ab}\left(C_{33}C_{44} - C_{xy}^2\right) + C_{ax}(C_{bx}C_{44} + C_{xy}C_{by}) \\ &\quad + C_{ay}(C_{bx}C_{xy} + C_{33}C_{by}) \\ &\approx C_{ab}C_xC_y + C_{ax}C_{bx}C_y + C_{ay}C_{by}C_x, \\ A_{22} &= C_{11}\left(C_{33}C_{44} - C_{xy}^2\right) - C_{ax}(C_{ax}C_{44} + C_{xy}C_{ay}) \\ &\quad - C_{ay}(C_{ax}C_{xy} + C_{33}C_{ay}) \approx C_aC_xC_y, \\ A_{23} &= C_{11}(C_{bx}C_{44} + C_{xy}C_{by}) + C_{ab}(C_{ax}C_{44} + C_{xy}C_{ay}) \\ &\quad + C_{ay}(C_{ax}C_{by} - C_{bx}C_{ay}) \approx C_{bx}C_aC_y, \end{aligned}$$

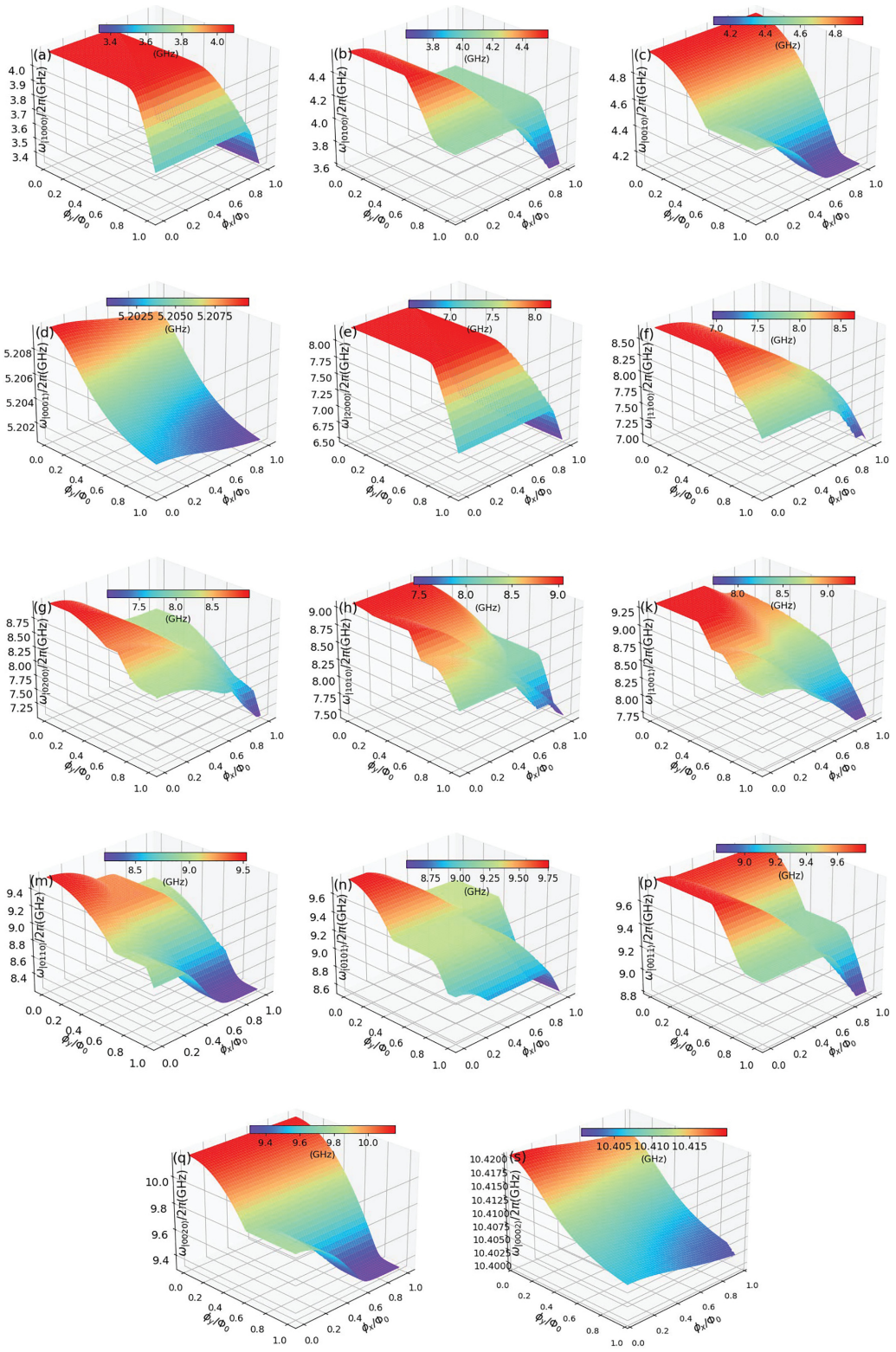

FIG. 10. The two-dimensional surfaces of energy levels. The curved surfaces for the single-excited state in the circuit are shown in (a)–(d), and (e)–(s) describe the energy-level curved surfaces of double-excited states. The maximal frequencies of two qubits are $\omega_x^{(\max)}/2\pi = 4.56$ GHz and $\omega_y^{(\max)}/2\pi = 5.12$ GHz. The other parameters are $g_{xy}/2\pi = 1$ MHz, $g_{ab}/2\pi = 0.1$ MHz, $\omega_a/2\pi = 4.10$ GHz, $\omega_b/2\pi = 5.20$ GHz, $\alpha_x/2\pi = -175$ MHz, $\alpha_y/2\pi = -195$ MHz, $g_{ax}/2\pi = g_{ay}/2\pi = 32$ MHz, and $g_{bx}/2\pi = g_{by}/2\pi = 30$ MHz.

$$
\begin{aligned}
A_{24} &= C_{11}(C_{bx}C_{xy} + C_{33}C_{by}) + C_{ab}(C_{ax}C_{xy} + C_{33}C_{ay}) \\
&\quad - C_{ax}(C_{ax}C_{by} - C_{bx}C_{ay}) \approx C_aC_xC_{by}, \\
A_{31} &= -C_{ab}(-C_{bx}C_{44} - C_{by}C_{xy}) + C_{ax}\left(C_{22}C_{44} - C_{by}^2\right) \\
&\quad - C_{ay}(-C_{22}C_{xy} - C_{bx}C_{by}) \approx C_{ax}C_bc_y, \\
A_{32} &= C_{11}(C_{bx}C_{44} + C_{by}C_{xy}) + C_{ax}(C_{ab}C_{44} + C_{ay}C_{by}) \\
&\quad + C_{ay}(C_{ab}C_{xy} - C_{bx}C_{by}) \approx C_{bx}C_aC_y, \\
A_{33} &= C_{11}\left(C_{22}C_{44} - C_{by}^2\right) + C_{ab}(-C_{ab}C_{44} - C_{ay}C_{by}) \\
&\quad - C_{ay}(C_{ab}C_{by} + C_{22}C_{ay}) \approx C_aC_bC_y, \\
A_{34} &= C_{11}(C_{22}C_{xy} + C_{bx}C_{by}) - C_{ab}(C_{ab}C_{xy} - C_{bx}C_{ay}) \\
&\quad + C_{ax}(C_{ab}C_{by} + C_{22}C_{ay}) \\
&\quad \approx C_{xy}C_aC_b + C_aC_{bx}C_{by} + C_bC_{ax}C_{ay}, \\
A_{41} &= C_{ab}(C_{bx}C_{xy} + C_{by}C_{33}) + C_{ax}(C_{22}C_{xy} + C_{bx}C_{by}) \\
&\quad + C_{ay}\left(C_{22}C_{33} - C_{bx}^2\right) \approx C_{ay}C_bC_x. \\
A_{42} &= C_{11}(C_{bx}C_{xy} + C_{by}C_{33}) + C_{ax}(C_{ab}C_{xy} - C_{ax}C_{by}) \\
&\quad - C_{ay}(-C_{ab}C_{33} - C_{ax}C_{bx}) \approx C_aC_xC_{by}, \\
A_{43} &= C_{11}(C_{22}C_{xy} + C_{bx}C_{by}) + C_{ab}(C_{ab}C_{xy} + C_{ax}C_{by}) \\
&\quad + C_{ay}(C_{ab}C_{bx} + C_{22}C_{ax}) \\
&\quad \approx C_{xy}C_aC_b + C_aC_{bx}C_{by} + C_bC_{ax}C_{ay}, \\
A_{44} &= C_{11}\left(C_{22}C_{33} - C_{bx}^2\right) + C_{ab}(-C_{ax}c_{33} - C_{ax}C_{bx}) \\
&\quad - C_{ax}(C_{ax}C_{bx} + C_{22}C_{ax}) \approx C_aC_bC_x. \qquad \text{(B5)}
\end{aligned}
$$

Thus, the Hamiltonian of the double-resonator couplers circuit can be expressed as

$$
\begin{aligned}
H &= 4E_{C_a}(n_a)^2 + 4E_{C_b}(n_b)^2 + 4E_{C_x}(n_x)^2 + 4E_{C_y}(n_y)^2 \\
&\quad + \frac{\phi_a^2}{2L_a} + \frac{\phi_b^2}{2L_b} - E_{J_x}\cos\left(\frac{2\pi}{\Phi_0}\phi_x\right) - E_{J_y}\cos\left(\frac{2\pi}{\Phi_0}\phi_y\right) \\
&\quad + 8\frac{C_{ax}}{\sqrt{C_aC_x}}\sqrt{E_{C_a}E_{C_x}}(n_an_x) + 8\frac{C_{ay}}{\sqrt{C_aC_y}}\sqrt{E_{C_a}E_{C_y}}(n_an_y) \\
&\quad + 8\frac{C_{bx}}{\sqrt{C_bC_x}}\sqrt{E_{C_b}E_{C_x}}(n_bn_x) + 8\frac{C_{by}}{\sqrt{C_bC_y}}\sqrt{E_{C_b}E_{C_y}}(n_bn_y) \\
&\quad + 8\left(1 + \frac{C_{ax}C_{bx}}{C_xC_{ab}} + \frac{C_{ay}C_{by}}{C_yC_{ab}}\right)\frac{C_{ab}}{\sqrt{C_aC_b}}\sqrt{E_{C_a}E_{C_b}}(n_an_b) \\
&\quad + 8\left(1 + \frac{C_{ax}C_{ay}}{C_aC_{xy}} + \frac{C_{bx}C_{by}}{C_bC_{xy}}\right)\frac{C_{xy}}{\sqrt{C_xC_y}}\sqrt{E_{C_x}E_{C_y}}(n_xn_y).
\end{aligned}
\qquad \text{(B6)}
$$

The two-body coupling strengths can be defined as

$$
g_{\lambda\beta} = \frac{1}{2}\frac{C_{\lambda\beta}}{\sqrt{C_\lambda C_\beta}}\sqrt{\omega_\lambda\omega_\beta}, \qquad \text{(B7)}
$$

$$
g_{ab} = \frac{1}{2}\left(1 + \frac{C_{ax}C_{bx}}{C_xC_{ab}} + \frac{C_{ay}C_{by}}{C_yC_{ab}}\right)\frac{C_{ab}}{\sqrt{C_aC_b}}\sqrt{\omega_a\omega_b}, \qquad \text{(B8)}
$$

$$
g_{xy} = \frac{1}{2}\left(1 + \frac{C_{ax}C_{ay}}{C_aC_{xy}} + \frac{C_{bx}C_{by}}{C_bC_{xy}}\right)\frac{C_{xy}}{\sqrt{C_xC_y}}\sqrt{\omega_x\omega_y}. \qquad \text{(B9)}
$$

The qubit-resonator interaction terms $g_{\lambda\beta}$ in Eq. (B9) could induce indirect coupling between two qubits, which should be decoupled to obtain the effective qubit-qubit coupling.

APPENDIX C: DECOUPLING PROCESSES

The Josephson energy of the Xmon qubit is much larger than its capacitance energy, $E_{J_\beta}/E_{C_\beta} \gg 1$, and then we can approximately get $\cos(\phi_\beta) = 1 - \phi_\beta^2/2 + \phi_\beta^4/24 - \cdots$. If we introduce the creation and annihilation operators by the definitions $\phi_\beta = \sqrt[4]{(2E_C/E_{J_\beta})}(a_\beta^\dagger + a_\beta)$ and $n_\beta = (i/2)\sqrt[4]{(2E_C/E_{J_\beta})}(a_\beta^\dagger - a_\beta)$, then the second quantized Hamiltonian can be obtained as $H_{\rm tot} = \sum_{\lambda=a,b} H_\lambda + \sum_{\beta=x,y} H_\beta + \sum_{\substack{\lambda=a,b\\ \beta=x,y}} H_{\lambda\beta} + H_{ab}^{(r)} + H_{xy}^{(q)}$, with

$$
H_\lambda = \frac{1}{2}\hbar\omega_\lambda c_\lambda^\dagger c_\lambda, \qquad \text{(C1)}
$$

$$
H_\beta = \frac{1}{2}\hbar\omega_\beta a_\beta^\dagger a_\beta + \frac{\alpha_\beta}{2}a_\beta^\dagger a_\beta^\dagger a_\beta a_\beta, \qquad \text{(C2)}
$$

$$
H_{\lambda\beta} = \hbar g_{\lambda\beta}(c_\lambda^\dagger a_\beta + c_\lambda a_\beta^\dagger - c_\lambda^\dagger a_\beta^\dagger - c_\lambda a_\beta), \qquad \text{(C3)}
$$

$$
H_{ab}^{(r)} = \hbar g_{ab}(c_a^\dagger c_b + c_a c_b^\dagger - c_a^\dagger c_b^\dagger - c_a c_b), \qquad \text{(C4)}
$$

$$
H_{xy}^{(q)} = \hbar g_{xy}(a_x^\dagger a_y + a_x a_y^\dagger - a_x^\dagger a_y^\dagger - a_x a_y). \qquad \text{(C5)}
$$

The transition frequencies of resonators and qubits are respectively defined as $\omega_\lambda = 1/\sqrt{C_\lambda L_\lambda}$ and $\omega_\beta = (\sqrt{8E_{J_\beta}E_{C_\beta}} - E_{C_\beta})/\hbar$, while $\alpha_\beta = -E_{C_\beta}/\hbar$ describes the anharmonicity of qubit β.

In the qubit-resonator dispersive coupling regimes, $g_{\lambda\beta}/|\Delta_{\lambda\beta}| \ll 1$, we can use the Schrieffer-Wolf transformation to decouple the variables of qubits and resonators. Since the resonator couplers are not pumped by the external fields, and the average cavity photon number should be much smaller than one, the virtual photon exchanges will dominate the cross-Kerr resonances. We define $S = \sum_{\substack{\lambda=a,b\\ \beta=x,y}}[(g_{\lambda\beta}/\Delta_{\lambda\beta})(c_\lambda^\dagger a_\beta - c_\lambda a_\beta^\dagger) - (g_{\lambda\beta}/\Sigma_{\lambda\beta})(c_\lambda^\dagger a_\beta^\dagger - c_\lambda a_\beta)]$. Under the unitary transformation $H^{(d)} = \exp(-S)H\exp(S)$, if we choose $H_{\lambda\beta} + [H_0, S] = 0$, then the decoupled Hamiltonian can be obtained as

$$
\begin{aligned}
H^{(d)} &= \hbar\omega_a^{(d)}c_a^\dagger c_a + \hbar\omega_b^{(d)}c_b^\dagger c_b + \hbar\omega_x^{(d)}a_x^\dagger a_x + \hbar\omega_y^{(d)}a_y^\dagger a_y \\
&\quad + \frac{\hbar\tilde{\alpha}_x}{2}a_x^\dagger a_x^\dagger a_x a_x + \frac{\hbar\tilde{\alpha}_y}{2}a_y^\dagger a_y^\dagger a_y a_y \\
&\quad + \hbar g_{xy}^{(d)}(a_x^\dagger a_y + a_y^\dagger a_x) + \hbar g_{ab}^{(d)}(c_a^\dagger c_b + c_b^\dagger c_a). \qquad \text{(C6)}
\end{aligned}
$$

The rotating wave approximation has been used to derive the above formula, and the constant terms were neglected. We also neglected the effects of small quantities (H_{xy} and H_{ab}). The anharmonicities of qubits are considered as invariant during unitary transformation ($\tilde{\alpha}_\beta \approx \alpha_\beta$), so some high-order effects relating to highly excited states of superconducting artificial atoms are neglected.

The transition frequencies of qubits, the resonant frequencies of resonators, the qubit-qubit coupling strength, and the resonator-resonator coupling strength in decoupled coordinates are obtained as

$$
\omega_x^{(d)} = \omega_x + \left(\frac{g_{ax}^2}{\Delta_{ax}} + \frac{g_{bx}^2}{\Delta_{bx}} - \frac{g_{ax}^2}{\Sigma_{ax}} - \frac{g_{bx}^2}{\Sigma_{bx}}\right), \qquad \text{(C7)}
$$

$$
\omega_y^{(d)} = \omega_y + \left(\frac{g_{ay}^2}{\Delta_{ay}} + \frac{g_{by}^2}{\Delta_{by}} - \frac{g_{ay}^2}{\Sigma_{ay}} - \frac{g_{by}^2}{\Sigma_{by}}\right), \qquad \text{(C8)}
$$

$$\omega_a^{(d)} = \omega_a - \left(\frac{g_{ax}^2}{\Delta_{ax}} + \frac{g_{ay}^2}{\Delta_{ay}} - \frac{g_{ax}^2}{\Sigma_{ax}} - \frac{g_{ay}^2}{\Sigma_{ay}}\right), \tag{C9}$$

$$\omega_b^{(d)} = \omega_b - \left(\frac{g_{bx}^2}{\Delta_{bx}} + \frac{g_{by}^2}{\Delta_{by}} - \frac{g_{bx}^2}{\Sigma_{bx}} - \frac{g_{by}^2}{\Sigma_{by}}\right), \tag{C10}$$

$$g_{xy}^{(d)} = \frac{1}{2}\left(\frac{g_{ax}g_{ay}}{\Delta_{ay}} + \frac{g_{bx}g_{by}}{\Delta_{by}} + \frac{g_{ay}g_{ax}}{\Delta_{ax}} + \frac{g_{by}g_{bx}}{\Delta_{bx}} - \frac{g_{ax}g_{ay}}{\Sigma_{ay}} - \frac{g_{bx}g_{by}}{\Sigma_{by}} - \frac{g_{ay}g_{ax}}{\Sigma_{ax}} - \frac{g_{by}g_{bx}}{\Sigma_{bx}}\right) + g_{xy}, \tag{C11}$$

$$g_{ab}^{(d)} = \frac{1}{2}\left(\frac{g_{ax}g_{bx}}{\Delta_{bx}} + \frac{g_{ay}g_{by}}{\Delta_{by}} + \frac{g_{bx}g_{ax}}{\Delta_{ax}} + \frac{g_{by}g_{ay}}{\Delta_{ay}} - \frac{g_{ax}g_{bx}}{\Sigma_{bx}} - \frac{g_{ay}g_{by}}{\Sigma_{by}} - \frac{g_{bx}g_{ax}}{\Sigma_{ax}} - \frac{g_{by}g_{ay}}{\Sigma_{ay}}\right) + g_{ab}. \tag{C12}$$

$g_{xy}^{(d)}$ is the decoupled qubit-qubit coupling strength, which can be used to analyze the switching off. $g_{ab}^{(d)}$ is the decoupled resonator-resonator and is much smaller than the frequency detuning between two resonators ($g_{ab}^{(d)} \ll |\Delta_{xy}|$), thus its contributions are neglected in this article.

APPENDIX D: CALCULATIONS OF HIGH-ENERGY-LEVEL CORRECTIONS

In the current theoretical model, the Kerr-nonlinear terms $H_{nl,\beta} = (\alpha_\beta/2)a_\beta^\dagger a_\beta^\dagger a_\beta a_\beta$ are assumed to be invariant ($\tilde{\alpha}_\beta \approx \alpha_\beta$) during the derivations of Eqs. (C6). This means that some high-order effects and the contributions of the highly excited state of the superconducting artificial atom are neglected, so the decoupled frequency and effective qubit-qubit coupling in Eqs. (C7)–(C12) contain no information on qubits' anharmonicities. But the anharmonicity of the Xmon qubit is very small, thus the resonator can couple to the highly excited states of atoms, which should affect the transition frequencies of qubits and the effective qubit-qubit coupling strengths. As discussed by some theoretical work, the anharmonicity could induced fourth-order self-Kerr and cross-Kerr resonances, and these effects could create corrections to the qubit's energy levels [31,32].

Bogoliubov transformation is used to analyze the higher-order effect during the decoupling processes for qubit-resonator interactions [32]. To maintain consistency, in this article we still use the Schrieffer-Wolf transformation to analyze the contributions of the Kerr-nonlinear terms $H_{nl,\beta}$ during the decoupling process. In the qubit-resonator dispersive coupling regimes, $(g_{\lambda\beta}/\Delta_{\lambda\beta}) \ll 1$ and $(g_{\lambda\beta}/\Sigma_{\lambda\beta}) \ll 1$, we define $S_{\lambda\beta} = (g_{\lambda\beta}/\Delta_{\lambda\beta})(c_\lambda^\dagger a_\beta - c_\lambda a_\beta^\dagger) - (g_{\lambda\beta}/\Sigma_{\lambda\beta})(c_\lambda^\dagger a_\beta^\dagger - c_\lambda a_\beta)$, where $S = \sum_{\substack{\lambda=a,b\\ \beta=x,y}} S_{\lambda\beta}$. Since $H_{nl,\beta}$ is a small quantity, we can separately conduct the unitary transform $H'_{nl,\beta} = \exp(S)H_{nl,\beta}\exp(-S)$ [32], thus we get

$$H'_{nl,\beta} = H_{nl,\beta} + [S, H_{nl,\beta}] + \frac{1}{2!}[S,[S,H_{nl,\beta}]] + \frac{1}{3!}[S[S,[S,H_{nl,\beta}]]] + \cdots. \tag{D1}$$

The commutation relation for the first-order expansion term

$$\begin{aligned}[S_{\lambda\beta}, H_{nl,\beta}] &= \left[\frac{g_{\lambda\beta}}{\Delta_{\lambda\beta}}(c_\lambda^\dagger a_\beta - c_\lambda a_\beta^\dagger) - \frac{g_{\lambda\beta}}{\Sigma_{\lambda\beta}}(c_\lambda^\dagger a_\beta^\dagger - c_\lambda a_\beta),\ \frac{\alpha_\beta}{2}a_\beta^\dagger a_\beta^\dagger a_\beta a_\beta\right] \\ &= \frac{g_{\lambda\beta}\alpha_\beta}{\Delta_{\lambda\beta}}(c_\lambda^\dagger a_\beta^\dagger a_\beta a_\beta + c_\lambda a_\beta^\dagger a_\beta^\dagger a_\beta) \\ &\quad + \frac{g_{\lambda\beta}\alpha_\beta}{\Sigma_{\lambda\beta}}(c_\lambda^\dagger a_\beta^\dagger a_\beta^\dagger a_\beta + c_\lambda a_\beta^\dagger a_\beta a_\beta).\end{aligned} \tag{D2}$$

Since $g_{xy}, g_{ab} \ll g_{\lambda\beta}$, we have neglected the effects of the weak direct qubit-qubit and resonator-resonator interactions.

The commutation relation for the second-order expansion term

$$\begin{aligned}[S_{\lambda\beta}, [S_{\lambda\beta}, H_{nl,\beta}]] &= \left[\frac{4g_{\lambda x}^2\alpha_\beta}{\Delta_{\lambda\beta}^2}c_\lambda^\dagger c_\lambda a_\beta^\dagger a_\beta + \frac{4g_{\lambda\beta}^2\alpha_\beta}{\Sigma_{\lambda\beta}^2}c_\lambda c_\lambda^\dagger a_\beta^\dagger a_\beta\right] \\ &\quad + \left(\frac{2g_{\lambda\beta}^2\alpha_\beta}{\Sigma_{\lambda\beta}^2} - \frac{2g_{\lambda\beta}^2\alpha_\beta}{\Delta_{\lambda\beta}^2}\right)a_\beta^\dagger a_\beta^\dagger a_\beta a_\beta \\ &\quad + \frac{g_{\lambda\beta}^2\alpha_\beta}{\Delta_{\lambda\beta}^2}c_\lambda^\dagger c_\lambda^\dagger a_\beta a_\beta + \frac{g_{\lambda\beta}^2\alpha_\beta}{\Delta_{\lambda\beta}^2}c_\lambda c_\lambda a_\beta^\dagger a_\beta^\dagger \\ &\quad + \frac{g_{\lambda\beta}^2\alpha_\beta}{\Sigma_{\lambda\beta}^2}c_\lambda^\dagger c_\lambda^\dagger a_\beta^\dagger a_\beta^\dagger + \frac{g_{\lambda\beta}^2\alpha_\beta}{\Sigma_{\lambda\beta}^2}c_\lambda c_\lambda a_\beta a_\beta \\ &\quad + \frac{2g_{\lambda\beta}^2\alpha_\beta}{\Delta_{\lambda\beta}\Sigma_{\lambda\beta}}c_\lambda^\dagger c_\lambda^\dagger a_\beta^\dagger a_\beta + \frac{4g_{\lambda\beta}^2\alpha_\beta}{\Delta_{\lambda\beta}\Sigma_{\lambda\beta}}c_\lambda c_\lambda a_\beta^\dagger a_\beta \\ &\quad + \frac{g_{\lambda\beta}^2\alpha_\beta}{\Delta_{\lambda\beta}\Sigma_{\lambda\beta}}(2c_\lambda^\dagger c_\lambda + 1)a_\beta a_\beta + \frac{g_{\lambda\beta}^2\alpha_\beta}{\Delta_{\lambda\beta}\Sigma_{\lambda\beta}}(2c_\lambda^\dagger c_\lambda + 1)a_\beta^\dagger a_\beta^\dagger.\end{aligned} \tag{D3}$$

Up to the second-order expanding terms, keeping the energy and particle number conservation terms, we can get the nonlinear term for qubit β in the decoupled coordinate as

$$\begin{aligned}H'_{nl,\beta} &= \sum_{\lambda=a,b}\left(\frac{g_{\lambda\beta}^2\alpha_\beta}{\Sigma_{\lambda\beta}^2} - \frac{g_{\lambda\beta}^2\alpha_\beta}{\Delta_{\lambda\beta}^2}\right)a_\beta^\dagger a_\beta^\dagger a_\beta a_\beta \\ &\quad + \sum_{\lambda=a,b}\left[\frac{2g_{\lambda x}^2\alpha_\beta}{\Delta_{\lambda\beta}^2}c_\lambda^\dagger c_\lambda a_\beta^\dagger a_\beta + \frac{2g_{\lambda\beta}^2\alpha_\beta}{\Sigma_{\lambda\beta}^2}c_\lambda c_\lambda^\dagger a_\beta^\dagger a_\beta\right] \\ &\quad + \sum_{\lambda=a,b}\left[\frac{g_{\lambda\beta}^2\alpha_\beta}{2\Delta_{\lambda\beta}^2}c_\lambda^\dagger c_\lambda^\dagger a_\beta a_\beta + \frac{g_{\lambda\beta}^2\alpha_\beta}{2\Delta_{\lambda\beta}^2}c_\lambda c_\lambda a_\beta^\dagger a_\beta^\dagger\right] \\ &\quad + \sum_{\lambda=a,b}\frac{g_{\lambda\beta}\alpha_\beta}{\Delta_{\lambda\beta}}(c_\lambda^\dagger a_\beta^\dagger a_\beta a_\beta + c_\lambda a_\beta^\dagger a_\beta^\dagger a_\beta).\end{aligned} \tag{D4}$$

In the right side of Eq. (D4), the first line describes the self-Kerr resonance, while the second line labels the cross-Kerr resonance. The third line describes the double virtual processes between one qubit and one resonator. The fourth line describes combined physical processes where the qubit and the resonator exchange a virtual photon, and the qubit simulatively participates in the self-excitation and subsequent self-annihilation processes.

[1] A. P. M. Place, L. V. H. Rodgers, P. Mundada, B. M. Smitham, M. Fitzpatrick, Z. Leng, A. Premkumar, J. Bryon, A. Vrajitoarea, S. Sussman, G. Cheng, T. Madhavan, H. K. Babla, X. Hoang Le, Y. Gang, B. Jäck, A. Gyenis, N. Yao, R. J. Cava, N. P. de Leon *et al.*, New material platform for superconducting transmon qubits with coherence times exceeding 0.3 milliseconds, Nat. Commun. **12**, 1779 (2021).

[2] C. Wang, X. Li, H. Xu, Z. Li, J. Wang, Z. Yang, Z. Mi, X. Liang, T. Su, C. Yang, G. Wang, W. Wang, Y. Li, M. Chen, C. Li, K. Linghu, J. Han, Y. Zhang, Y. Feng, Y. Song *et al.*, Towards practical quantum computers: Transmon qubit with a lifetime approaching 0.5 milliseconds, npj Quantum Inf. **8**, 3 (2022).

[3] W. Ren, W. Li, S. Xu, K. Wang, W. Jiang, F. Jin, X. Zhu, J. Chen, Z. Song, P. Zhang, H. Dong, X. Zhang, J. Deng, Y. Gao, C. Zhang, Y. Wu, B. Zhang, Q. Guo, H. Li, Z. Wang *et al.*, Experimental quantum adversarial learning with programmable superconducting qubits, Nat. Comput. Sci. **2**, 711 (2022).

[4] S. Xu, Z.-Z. Sun, K. Wang, L. Xiang, Z. Bao, Z. Zhu, F. Shen, Z. Song, P. Zhang, W. Ren, X. Zhang, H. Dong, J. Deng, J. Chen, Y. Wu, Z. Tan, Y. Gao, F. Jin, X. Zhu, C. Zhang *et al.*, Digital simulation of non-Abelian anyons with 68 programmable superconducting qubits, Chin. Phys. Lett. **40**, 060301 (2023).

[5] M. Bal, A. A. Murthy, S. Zhu, F. Crisa, X. You, Z. Huang, T. Roy, J. Lee, D. v. Zanten, R. Pilipenko, I. Nekrashevich, D. Bafia, Y. Krasnikova, C. J. Kopas, E. O. Lachman, D. Miller, J. Y. Mutus, M. J. Reagor, H. Cansizoglu, J. Marshall *et al.*, Systematic improvements in transmon qubit coherence enabled by niobium surface encapsulation, arXiv:2304.13257 (2023).

[6] Y. Chen, C. Neill, P. Roushan, N. Leung, M. Fang, R. Barends, J. Kelly, B. Campbell, Z. Chen, B. Chiaro, A. Dunsworth, E. Jeffrey, A. Megrant, J. Y. Mutus, P. J. J. ÓMalley, C. M. Quintana, D. Sank, A. Vainsencher, J. Wenner, T. C. White *et al.*, Qubit architecture with high coherence and fast tunable coupling, Phys. Rev. Lett. **113**, 220502 (2014).

[7] F. Yan, P. Krantz, Y. Sung, M. Kjaergaard, D. L. Campbell, T. P. Orlando, S. Gustavsson, and W. D. Oliver, Tunable coupling scheme for implementing high-fidelity two-qubit gates, Phys. Rev. Appl. **10**, 054062 (2018).

[8] X. Li, T. Cai, H. Yan, Z. Wang, X. Pan, Y. Ma, W. Cai, J. Han, Z. Hua, X. Han, Y. Wu, H. Zhang, H. Wang, Y. Song, L. Duan, and L. Sun, Tunable coupler for realizing a controlled-phase gate with dynamically decoupled regime in a superconducting circuit, Phys. Rev. Appl. **14**, 024070 (2020).

[9] Y. Xu, J. Chu, J. Yuan, J. Qiu, Y. Zhou, L. Zhang, X. Tan, Y. Yu, S. Liu, J. Li, F. Yan, and D. Yu, High-fidelity, high-scalability two-qubit gate scheme for superconducting qubits, Phys. Rev. Lett. **125**, 240503 (2020).

[10] J. Stehlik, D. M. Zajac, D. L. Underwood, T. Phung, J. Blair, S. Carnevale, D. Klaus, G. A. Keefe, A. Carniol, M. Kumph, M. Steffen, and O. E. Dial, Tunable coupling architecture for fixed-frequency transmon superconducting qubits, Phys. Rev. Lett. **127**, 080505 (2021).

[11] I. N. Moskalenko, I. A. Simakov, N. N. Abramov, A. A. Grigorev, D. O. Moskalev, A. A. Pishchimova, N. S. Smirnov, E. V. Zikiy, I. A. Rodionov, and I. S. Besedin, High fidelity two-qubit gates on fluxoniums using a tunable coupler, npj Quantum Inf. **8**, 130 (2022).

[12] A. Kandala, K. X. Wei, S. Srinivasan, E. Magesan, S. Carnevale, G. A. Keefe, D. Klaus, O. Dial, and D. C. McKay, Demonstration of a high-fidelity CNOT gate for fixed-frequency transmons with engineered ZZ suppression, Phys. Rev. Lett. **127**, 130501 (2021).

[13] Q. Zhu, S. Cao, F. Chen, M.-C. Chen, X. Chen, T.-H. Chung, H. Deng, Y. Du, D. Fan, M. Gong, C. Guo, C. Guo, S. Guo, L. Han, L. Hong, H.-L. Huang, Y.-H. Huo, L. Li, N. Li, S. Li *et al.*, Quantum computational advantage via 60-qubit 24-cycle random circuit sampling, Sci. Bull. **67**, 240 (2022).

[14] F. Arute, K. Arya, R. Babbush, D. Bacon, J. C. Bardin, R. Barends, R. Biswas, S. Boixo, F. G. S. L. Brandao, D. A. Buell, B. Burkett, Y. Chen, Z. Chen, B. Chiaro, R. Collins, W. Courtney, A. Dunsworth, E. Farhi, B. Foxen, A. Fowler *et al.*, Quantum supremacy using a programmable superconducting processor, Nature (London) **574**, 505 (2019).

[15] Y. Wu, W.-S. Bao, S. Cao, F. Chen, M.-C. Chen, X. Chen, T.-H. Chung, H. Deng, Y. Du, D. Fan, M. Gong, C. Guo, C. Guo, S. Guo, L. Han, L. Hong, H.-L. Huang, Y.-H. Huo, L. Li, N. Li *et al.*, Strong quantum computational advantage using a superconducting quantum processor, Phys. Rev. Lett. **127**, 180501 (2021).

[16] Y. Sung, L. Ding, J. Braumüller, A. Vepsäläinen, B. Kannan, M. Kjaergaard, A. Greene, G. O. Samach, C. McNally, D. Kim, A. Melville, B. M. Niedzielski, M. E. Schwartz, J. L. Yoder, T. P. Orlando, S. Gustavsson, and W. D. Oliver, Realization of high-fidelity CZ and ZZ-free ISWAP gates with a tunable coupler, Phys. Rev. X **11**, 021058 (2021).

[17] H. Wang, Y.-J. Zhao, R. Wang, X.-W. Xu, Q. Liu, J. Wang, and C. Jin, Frequency adjustable resonator as a tunable coupler for Xmon qubits, J. Phys. Soc. Jpn. **91**, 104005 (2022).

[18] M. Gong, S. Wang, C. Zha, M.-C. Chen, H.-L. Huang, Y. Wu, Q. Zhu, Y. Zhao, S. Li, S. Guo, H. Qian, Y. Ye, F. Chen, C. Ying, J. Yu, D. Fan, D. Wu, H. Su, H. Deng, H. Rong *et al.*, Quantum walks on a programmable two-dimensional 62-qubit superconducting processor, Science **372**, 948 (2021).

[19] IBM-Q-Team, IBM-Q-53 Rochester backend specification v1.2.0 (2020).

[20] Y. Wu, L.-P. Yang, M. Gong, Y. Zheng, H. Deng, Z. Yan, Y. Zhao, K. Huang, A. D. Castellano, W. J. Munro, K. Nemoto, D.-N. Zheng, C. P. Sun, Yu-xi Liu, X. Zhu, L. Lu, An efficient and compact switch for quantum circuits, npj Quantum Inf. **4**, 50 (2018).

[21] D. C. McKay, S. Filipp, A. Mezzacapo, E. Magesan, J. M. Chow, and J. M. Gambetta, Universal gate for fixed-frequency qubits via a tunable bus, Phys. Rev. Appl. **6**, 064007 (2016).

[22] P. Mundada, G. Zhang, T. Hazard, and A. Houck, Suppression of qubit crosstalk in a tunable coupling superconducting circuit, Phys. Rev. Appl. **12**, 054023 (2019).

[23] H. Goto, Double-transmon coupler: Fast two-qubit gate with no residual coupling for highly detuned superconducting qubits, Phys. Rev. Appl. **18**, 034038 (2022).

[24] E. A. Sete, A. Q. Chen, R. Manenti, S. Kulshreshtha, and S. Poletto, Floating tunable coupler for scalable quantum computing architectures, Phys. Rev. Appl. **15**, 064063 (2021).

[25] J. R. Johansson, P. D. Nation, and F. Nori, QUTIP 2: A Python framework for the dynamics of open quantum systems, Comput. Phys. Commun. **184**, 1234 (2013).

[26] J. R. Johansson, P. D. Nation, and F. Nori, QUTIP: An open-source Python framework for the dynamics of open quantum systems, Comput. Phys. Commun. **183**, 1760 (2012).

[27] H. Sun, Tunable Coupler in Superconducting Circuits and Impedance Engineering for Josephson Parametric Amplifier, MS thesis, University of Waterloo (2020).

[28] N. J. Glaser, F. Roy, and S. Filipp, Controlled-controlled-phase gates for superconducting qubits mediated by a shared tunable coupler, Phys. Rev. Appl. **19**, 044001 (2023).

[29] M. H. Devoret, *Quantum Fluctuations in Electrical Circuits* (Elsevier, 1997).

[30] S. M. Girvin, Superconducting qubits and circuits: Artificial atoms coupled to microwave photons, in *Lecture Notes delivered at Les Houches Summer School* (Oxford University Press, 2011).

[31] G. Zhu, D. G. Ferguson, V. E. Manucharyan, and J. Koch, Circuit QED with fluxonium qubits: Theory of the dispersive regime, Phys. Rev. B **87**, 024510 (2013).

[32] A. Blais, A. L. Grimsmo, S. M. Girvin, and A. Wallraff, Circuit quantum electrodynamics, Rev. Mod. Phys. **93**, 025005 (2021).

[33] P. Zhao, K. Linghu, Z. Li, P. Xu, R. Wang, G. Xue, Y. Jin, and H. Yu, Quantum crosstalk analysis for simultaneous gate operations on superconducting qubits, PRX Quantum **3**, 020301 (2022).

[34] A. C. Santos, Role of parasitic interactions and microwave crosstalk in dispersive control of two superconducting artificial atoms, Phys. Rev. A **107**, 012602 (2023).

[35] P. Zhao, P. Xu, D. Lan, J. Chu, X. Tan, H. Yu, and Y. Yu, High-contrast ZZ interaction using superconducting qubits with opposite-sign anharmonicity, Phys. Rev. Lett. **125**, 200503 (2020).

[36] J. Ku, X. Xu, M. Brink, David C. McKay, Jared B. Hertzberg, M. H. Ansari, and B. L. T. Plourde, Suppression of unwanted ZZ interactions in a hybrid two-qubit system, Phys. Rev. Lett. **125**, 200504 (2020).

[37] F. Marxer, A. Vepsäläinen, S. W. Jolin, J. Tuorila, A. Landra, C. Ockeloen-Korppi, W. Liu, O. Ahonen, A. Auer, L. Belzane, V. Bergholm, Chun F. Chan, K. W. Chan, T. Hiltunen, J. Hotari, E. Hyyppä, J. Ikonen, D. Janzso, M. Koistinen, J. Kotilahti *et al.*, Long-distance transmon coupler with CZ-gate fidelity above 99.8%, PRX Quantum **4**, 010314 (2023).

[38] C. Leroux, A. D. Paolo, and A. Blais, Superconducting coupler with exponentially large on-off ratio, Phys. Rev. Appl. **16**, 064062 (2021).

[39] R. Krishnan and J. A. Pople, Approximate fourth-order perturbation theory of the electron correlation energy, Int. J. Quantum Chem. **14**, 91 (1978).